CRYSTAL GROWTH & DESIGN

pubs.acs.org/crystal

Article

Synthesis and Characterization of Xylazine Hydrochloride Polymorphs, Hydrates, and Cocrystals: A ^{35}Cl Solid-State NMR and DFT Study

Louae M. Abdulla,[‖] Austin A. Peach,[‖] Sean T. Holmes,[‖] Zachary T. Dowdell, Lara K. Watanabe, Emilia M. Iacobelli, David A. Hirsh, Jeremy M. Rawson, and Robert W. Schurko*

Cite This: *Cryst. Growth Des.* 2023, 23, 3412−3426

Read Online

ACCESS | Metrics & More | Article Recommendations | Supporting Information

ABSTRACT: Xylazine HCl (X) is a veterinary analgesic with many known solid forms, making it an ideal system for studying the noncovalent interactions, such as hydrogen bonding, that provide stability to polymorphs, solvates/hydrates, and cocrystal of pharmaceuticals. Herein, we report methods for the reliable preparation and interconversion of polymorphs of X (including mechanochemical pathways), the discovery of a novel polymorph, and the synthesis of three cocrystals with coformers containing amide and carboxylic acid moieties. An understanding of ball milling protocols is essential for optimizing these reactions and ensuring clean and reproducible syntheses of the products in high yields. All materials were characterized using thermal analysis, powder and single-crystal X-ray diffraction (PXRD and SCXRD), and multinuclear solid-state NMR (SSNMR) spectroscopy. ^{35}Cl SSNMR is highlighted for its versatility for fingerprinting polymorphs, hydrates, and cocrystals (including the detection of impurity phases that are not always evident from PXRD and offering an avenue for optimizing synthetic protocols) and providing molecular-level structural information. The ^{35}Cl electric field gradient (EFG) tensor is extremely sensitive to the unique hydrogen-bonding network in each solid form of X, resulting in distinct powder patterns. Dispersion-corrected plane-wave density functional theory (DFT) structural refinements yield better models of the hydrogen-bonding environments of the chloride ions than is possible through XRD methods alone. Calculations employing the refined structures yield ^{35}Cl EFG tensors that agree well with experiment. PXRD and ^{35}Cl SSNMR, in tandem with reliable calculations of EFG tensors, are essential for the development of NMR crystallographic and crystal structure prediction protocols and crucial for future studies involving HCl salts and their concomitant solid forms.

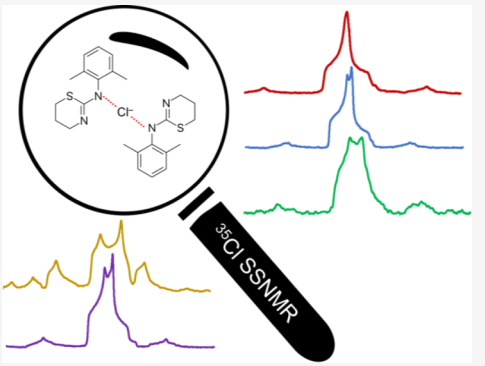

1. INTRODUCTION

The physicochemical properties of active pharmaceutical ingredients (APIs), including stability, solubility, bioavailability, and reactivity, depend on the structures of their solid forms,[1−12] which include salts, polymorphs, hydrates/solvates, cocrystals, amorphous solid dispersions, and combinations thereof.[13−16] The synthesis of polymorphs (*i.e.*, different crystalline forms containing the same molecular components), salts (*i.e.*, solids exhibiting complete charge transfer between two or more components), hydrates/solvates (*i.e.*, solids in which water/solvent molecules are incorporated into the crystal lattice), and/or cocrystals (*i.e.*, solids that are composed of two or more molecular and/or ionic components in the same crystal lattice, which are neither solvates nor simple salts) affords additional opportunities for enhancing desired physicochemical properties of pharmaceutical products. Given the importance of the production of solid forms of APIs to the pharmaceutical industry, the propensity of neutral organic molecules and their salts to exhibit polymorphism, as well as cocrystal and hydrate/solvate formation, has been evaluated through mining of databases and quantum chemical calculations.[17−20] Furthermore, the potential for tailoring the physicochemical properties of APIs through the production of a variety of different solid forms is crucial for the design and manufacture of dosage formulations of high efficacy, and may even provide insight into the rational design of new solid forms.

Intermolecular noncovalent interactions in solid APIs that influence their structure and concomitant physicochemical properties are of great interest. In particular, understanding H···Cl$^-$ hydrogen bonding is very important since nearly half of all commercial pharmaceuticals are constituted by hydrochloride (HCl) salts of APIs.[21] In HCl salts, H···Cl$^-$ hydrogen-bonding interactions are a major source of structural stability

Received: December 28, 2022
Revised: March 30, 2023
Published: April 21, 2023

https://doi.org/10.1021/acs.cgd.2c01539
Cryst. Growth Des. 2023, 23, 3412−3426

since the chloride ions can accommodate multiple hydrogen bonds, leading to a wide variety of structural arrangements. Furthermore, the presence of solvent molecules (most commonly water) and/or coformer molecules (in the case of cocrystals) can impact the properties of HCl APIs through the formation of new types of H···Cl^- hydrogen bonds. Therefore, an understanding of H···Cl^- hydrogen-bonding interactions allows for informed choice of solvents and coformers, which is paramount for the rational design of new solid forms with specifically tailored physicochemical properties.

Key to the successful production of polymorphs, hydrates, and cocrystals of APIs is a reliable and rapid means of molecular-level structural characterization. Characterization methods such as powder and single-crystal X-ray diffraction (PXRD and SCXRD, respectively) thermal analysis, vibrational spectroscopy (IR and Raman), and solid-state NMR (SSNMR) spectroscopy all play important roles in this respect.[22,23] Of these, SSNMR spectroscopy is the premier technique for providing atomic-level structural detail. One-dimensional (1D) and two-dimensional (2D) ^{13}C, ^{15}N, ^{19}F, and ^{1}H SSNMR experiments are commonly used to characterize the molecular structures of APIs and are well suited for exploring noncovalent interactions that are key in determining the arrangements of the molecules in different solid forms.[23−29]

Our group and others have demonstrated that ^{35}Cl SSNMR spectroscopy is invaluable for rapid fingerprinting and differentiation of different solid forms of the APIs in both bulk and dosage forms, as well as probing the local geometries of ions, including the types, numbers, and arrangements of chemical species participating in H···Cl^- hydrogen bonding.[30−57] The ^{35}Cl SSNMR spectra of chloride ions in organic HCl salts almost always feature broad central-transition (CT, $+1/2 \leftrightarrow -1/2$) powder patterns that are influenced by the second-order quadrupolar interaction (SOQI), and in many cases, chlorine chemical shift anisotropy (CSA). The ^{35}Cl electric field gradient (EFG) tensor, which gives rise to the QI, is extremely sensitive to changes and/or differences in chloride ion environments that result from distinct hydrogen-bonding arrangements. Different solid forms of APIs have distinct arrangements of H···Cl^- hydrogen bonds, with hydrates and cocrystals even featuring additional types of hydrogen bonds involving water molecules or coformers, respectively. Accordingly, ^{35}Cl SSNMR spectroscopy is a robust tool for the structural characterization of solid forms of APIs, including their polymorphs, hydrates, and cocrystals.

Xylazine HCl, (2-(2,6-xylidino)-5,6-dihydro-4*H*-1,3-thiazine hydrochloride), denoted here as X, is used as a sedative, analgesic, and muscle relaxant in veterinary medicine (Scheme 1).[58] There are five reported solid forms of X that can be produced under ambient conditions, including one hydrate (**Xh**) and four anhydrous polymorphs (**Xx**, **Xa**, **Xz**, and **Xm**), the crystal structures of which have been reported for all forms except **Xm**.[59−61] There are additional hydrates and solvates that can be made under conditions of high pressure;[61] however, these will not be discussed in the current study. There are reports that the anhydrous forms of X slowly convert into **Xh** under ambient conditions, and can rapidly convert into **Xh** under controlled environmental conditions (*i.e.*, hydration chamber or recrystallization from water).[61] Furthermore, **Xh** can be used as a reagent in the synthesis of the anhydrous polymorphs **Xx**, **Xa**, and **Xz** under various synthetic conditions (*i.e.*, heating under vacuum, recrystallization, *etc.*).[59,62,63] This complex array of interconversions between the reported hydrated and anhydrous forms (Scheme 2) makes these systems ideal for a case study of polymorph discovery and/or interconversion, hydration state identification, as well as for exploring accelerated mechanochemical interconversions and cocrystal design.

Scheme 1. Molecular Structure of Xylazine HCl

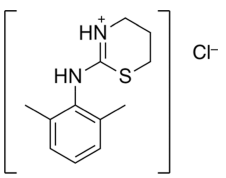

Herein, we discuss the synthesis, characterization, and structural refinement of a monohydrate, three known polymorphs, one novel polymorph, and three novel cocrystals of X (Table 1). In all cases, solid forms of X are characterized with a combination of PXRD, SCXRD, DSC, TGA, and multinuclear SSNMR spectroscopy (^{13}C and ^{35}Cl). First, we discuss the reported and novel mechanochemical syntheses of **Xh**, **Xx**, **Xa**, and **Xz**, and demonstrate specific pathways for their interconversion. Second, utilizing information garnered from similar crystal systems and accompanying PXRD and ^{35}Cl SSNMR data, ball milling protocols are used to synthesize the new polymorph **Xy** and three cocrystals of X with benzoic acid (Bzc) and benzamide (Bza) in 1:1 ratios (**XBzc** and **XBza**) and malonic acid (Mal) in a 2:1 ratio (**X_2Mal**). We also report crystal structures from SCXRD for the novel polymorph and cocrystals. ^{35}Cl SSNMR spectroscopy provides a unique spectral fingerprint for each solid form of X (and cocrystals), which is associated with unique sets of chlorine EFG and chemical shift (CS) tensors. Third, dispersion-corrected plane-wave DFT (DFT-D2*) methods are used to refine all crystal structures, with the validity of the structures assessed *via* comparison of experimental and calculated ^{35}Cl EFG tensors. Relationships between the local chloride hydrogen-bonding environments and the ^{35}Cl EFG tensor parameters and orientations are also investigated. Finally, the future application of quadrupolar NMR-based crystallography and crystal structure prediction of APIs, polymorphs, hydrates, and cocrystals is discussed briefly.

2. EXPERIMENTAL SECTION

2.1. Materials. Samples of X, Bzc, and Mal were purchased from Millipore Sigma. Bza was purchased from Oakwood Chemical. PXRD indicates that different batches of the as-received samples of X consist either of pure phases of **Xz** or **Xa**, or as a mixture of **Xz** and **Xh** (*vide infra*). All other reagents consist of pure phases. Solvents, including methanol (MeOH), ethanol (EtOH), acetonitrile (MeCN), dimethylformamide (DMF), and dichloromethane (DCM), were purchased from VWR. All powder samples were stored in 20 mL glass vials, sealed with plastic screw caps, and stored under conditions of controlled relative humidity (except for **Xx**, which was transferred and packed in a glovebox to minimize contact with air/water).

2.2. Mechanochemical Synthesis. All ball mill syntheses involved liquid-assisted grinding (LAG) or neat grinding (NG) using a Retsch Mixer Mill 400 at a milling frequency of 20 Hz for 90 min. All educts were placed in a vacuum oven overnight prior to their usage to minimize surface water absorption. The materials were placed in a 10 mL Teflon milling jar with two 5 mm stainless steel ball bearings. Materials used for LAG synthesis were added to the milling jars prior to the addition of solvent. Parameters used in the mechanochemical syntheses can be found in Tables S1 and S2

https://doi.org/10.1021/acs.cgd.2c01539
Cryst. Growth Des. 2023, 23, 3412−3426

Scheme 2. Summary of Previously Reported Reaction Pathways for the Synthesis of Xylazine HCl (X) Anhydrous Polymorphs and the Monohydrate: (i) Formation of Xh through Slow Recrystallization of Xa, Xm, Xx, or Xz from Water or Placement in Hydration Chamber; (ii) Heating at (a) 100 °C for 2 Days and (b) 60 °C for 1 Day in a Vacuum Oven, to Synthesize Xa and Xx, Respectively; (iii) Recrystallization of Xa from Methanol to Obtain Xz, or Recrystallization from DCM to Form Xm (Following the Desolvation of an Intermediate Phase)

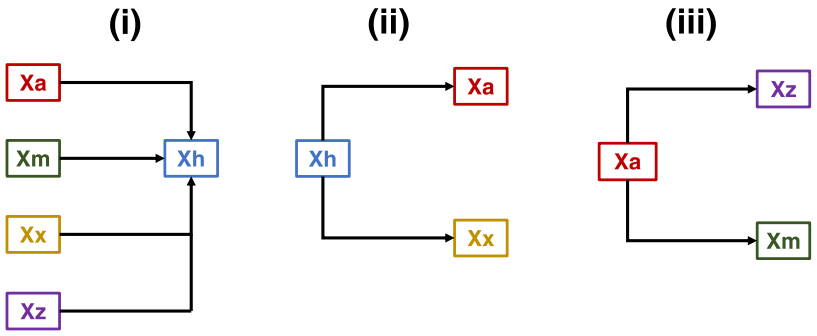

Table 1. Summary of Solid Forms of Xylazine HCl, Abbreviated Names Used in This Work, and an Overview of Crystallographic Data

form of xylazine HCl	abbreviation	space group	Z, Z'	refs
monohydrate	**Xh**	$P2_1/c$	4, 1	this work
form A	**Xa**	$P2_1/c$	4, 1	59
form X	**Xx**	$P2_1/c$	4, 1	59
form Z	**Xz**	$P2_1/c$	4, 1	59
form M	**Xm**	unknown	unknown	n/a
form Y	**Xy**	$P6_1$	6, 1	this work
benzoic acid 1:1 cocrystal	**XBzc**	$C2/c$	8, 1	this work
benzamide 1:1 cocrystal	**XBza**	$P\bar{1}$	2, 1	this work
malonic acid 2:1 cocrystal	**X_2Mal**	$P2_12_12_1$	4, 1	this work

(Supporting Information). Mechanochemical interconversions between the different polymorphs and hydrate of X were all completed by LAG methods. The starting material and solvent were placed in Teflon jars and milled in the presence of two 5 mm stainless steel or 3 Å 4−8 mesh molecular sieves as ball bearings. Syntheses of the **XBzc**, **XBza**, and **X_2Mal** PCCs were completed by NG, in a 1:1 ratio using any form of X and coformers Bza or Bzc, or a 2:1 ratio of X and Mal. No further grinding of samples was done prior to packing into plate sample holders for analysis by PXRD or glass tubes/zirconia rotors for analysis by SSNMR.

2.3. Powder X-ray Diffraction. PXRD patterns for all samples were acquired using a Proto AXRD benchtop diffractometer with a Cu Kα radiation source and a DECTRIS hybrid pixel detector using the XRDWin software. Samples were mounted on plate sample holders manufactured by Proto. The X-ray tube voltage and current were 30 kV and 20 mA, respectively. The divergence and scattering slits were set to 0.5 and 0.6 mm, respectively. Diffraction experiments were run with the detector scanning a 2θ range from 5 to 45° implementing a dwell time of 10 seconds, resulting in *ca.* 55 min of acquisition time per sample. Additional confirmations of sample identities and purities were obtained *via* PXRD experiments conducted using a Rigaku Miniflex benchtop diffractometer with a Cu Kα radiation source and D/tex Ultra silicon strip detector. The X-ray tube voltage and current were set to 40 kV and 15 mA, respectively. All samples were packed in zero-background silicon wafers with a well size of 5 mm × 0.2 mm mounted on an eight-position autosampler. Diffraction experiments were run with the detector scanning 2θ angles from 5 to 50° with a step size of 0.03° and speed of 5° min^{-1} (acquisition time of *ca.* 10 min). The resulting PXRD patterns for all samples were compared to single-crystal simulations for purity assessment and identification of starting reagents and final products, using the CrystalDiffract software package.

2.4. Single-Crystal X-ray Diffraction. Crystals were coated in paratone-*N* oil and mounted onto a goniometer head using a polyimide cryoloop. The crystals were mounted and cooled to 170 ± 2 K using an Oxford Cryosystems Cryostat (700 Series Cryostream Plus) attached to the diffractometer. X-ray reflections were collected and integrated from frame data using the APEX-III[64] software suite on a Bruker D8 Venture four-circle diffractometer equipped with a Photon CCD detector utilizing a graphite monochromator with either Cu Kα (λ = 1.54178 Å) or Mo Kα radiation (λ = 0.71073 Å). The SAINT[64] software package was used for raw area detector data frame reductions and SADABS[64] was used for absorption corrections (multiscan; semiempirical from equivalents). Structures were solved using intrinsic phasing[65] and refined against F^2 with SHELXL[66] software implemented within the OLEX2[67] program. The refinement of all nonhydrogen atoms was completed anisotropically. In all structures, hydrogens attached to N2 and N4 were identified in difference electron density maps, while all other hydrogen atoms were located in idealized positions and refined using a riding model. The structures have been deposited on the Cambridge Structural Database with CSD deposition numbers 2214351−2214355.

2.5. Thermal Analysis. Thermogravimetric analysis (TGA) studies were conducted using a TA Instruments TGA5500. Differential scanning calorimetry (DSC) studies were conducted using a TA Instruments DSC2500. N_2 gas with 99.999% purity was used to purge the systems at a flow rate of 60 mL min^{-1}. Samples (*ca.* 5 mg) were placed in aluminum pans and referenced against an empty pan for the DSC measurements. TGA samples were held at 25 °C for 5 min before heating to 500 °C at a rate of 5 °C min^{-1}.

2.6. Solid-State Nuclear Magnetic Resonance Spectroscopy. *2.6.1. Overview.* All moderate-field SSNMR experiments were conducted at the University of Windsor (Windsor, Ontario) and acquired using a Bruker Avance III HD NMR spectrometer with an Oxford wide-bore magnet with resonance frequencies of $\nu_0(^{13}C)$ = 100.64 MHz, $\nu_0(^{1}H)$ = 400.224 MHz, and $\nu_0(^{35}Cl)$ = 39.21 MHz. Static experiments were conducted using a revolution 5 mm HX ultra-low temperature stationary probe with samples packed into 5 mm outer diameter (o.d.) glass tubes sealed with Teflon tape. Magic-angle spinning (MAS) NMR experiments were conducted using a Varian/Chemagnetics 4 mm HX MAS probe with samples packed into 4 mm o.d. zirconia rotors with a Teflon cap. All high-field SSNMR experiments were conducted at the National High Magnetic Field Laboratory (Tallahassee, Florida). Samples of **Xz**, **Xx**, **Xa**, and **Xh** were packed into 3.2 mm o.d. zirconia rotors and acquired under static and MAS conditions using a Bruker Avance III HD spectrometer, a 31 mm bore Oxford magnet, and a home-built 3.2 mm HX MAS probe (B_0 =19.5 T, $\nu_0(^{1}H)$ = 831.48 MHz, and $\nu_0(^{35}Cl)$ = 81.46 MHz). Samples of **XBza**, **XBzc**, **X_2Mal**, and **Xy** were

https://doi.org/10.1021/acs.cgd.2c01539
Cryst. Growth Des. 2023, 23, 3412−3426

Table 2. Experimental and Calculated ^{35}Cl EFG and Chemical Shift Tensor Parameters of Xylazine HCl Polymorphs, Hydrates, and Cocrystals[a,b,c,d,e]

material		C_Q (MHz)	η_Q	δ_{iso} (ppm)	Ω (ppm)	κ	α (deg.)	β (deg.)	γ (deg.)
Xh	exp.	3.59(6)	0.80(4)	76(4)	65(10)	0.0(4)	80(10)	75(5)	5(10)
	RPBE-D2*	3.80	0.53	80	62	−0.27	99	82	8
	SCXRD	2.53	0.53	49	41	−0.31	101	81	18
Xa	exp.	3.29(6)	0.87(4)	131(5)	110(30)	0.5(4)	0(10)	10(10)	95(5)
	RPBE-D2*	−3.56	0.63	141	132	0.87	168	5	124
	PXRD	2.70	0.92	128	134	0.49	109	89	12
Xx	exp.	5.28(6)	0.28(4)	79(5)	150(20)	0.1(2)	0(10)	5(10)	100(5)
	RPBE-D2*	−4.72	0.50	76	148	−0.32	101	4	13
	PXRD	2.90	0.88	71	121	−0.63	100	90	4
Xy	exp.	6.15(8)	0.14(5)	79(5)	120(50)	[f]	[f]	0(30)	[f]
	RPBE-D2*	−6.08	0.17	95	148	0.71	65	4	16
	SCXRD	−2.75	0.64	68	106	0.73	5	5	37
Xz	exp.	3.94(5)	0.64(4)	80(4)	80(30)	−0.7(2)	165(10)	90(10)	0(30)
	RPBE-D2*	−3.40	0.99	87	120	−0.64	161	9	76
	PXRD	−2.92	0.93	86	105	−0.69	55	17	48
XBzc	exp.	5.23(6)	0.50(4)	107(5)	140(30)	0.0(4)	20(10)	25(10)	95(10)
	RPBE-D2*	−5.22	0.68	112	144	−0.03	15	30	98
	SCXRD	−2.57	0.07	78	111	−0.06	41	29	106
XBza	exp.	5.35(5)	0.51(3)	91(4)	100(30)	[f]	[f]	0(10)	[f]
	RPBE-D2*	−5.06	0.60	89	96	0.15	33	9	121
	SCXRD	−2.32	0.63	57	65	−0.15	52	18	34
X_2Mal (Cl1)	exp.	4.28(8)	0.30(5)	92(5)	50(30)	[f]	[f]	0(10)	[f]
	RPBE-D2*	3.98	0.35	109	47	−0.10	147	69	30
	SCXRD	3.07	0.66	79	34	−0.86	141	69	117
X_2Mal (Cl2)	exp.	4.73(8)	0.97(5)	127(5)	100(50)	[f]	85(20)	85(20)	[f]
	RPBE-D2*	4.93	0.91	144	95	−0.09	115	88	24
	SCXRD	2.13	0.44	99	43	−0.22	116	87	41

[a]Theoretical EFG and CS tensor parameters were obtained from calculations on XRD-derived structures and structures refined at the RPBE-D2* level. [b]The experimental uncertainties in the last digit for each value are indicated in parentheses. [c]The principal components of the EFG tensors are defined such that $|V_{33}| \geq |V_{22}| \geq |V_{11}|$. The quadrupolar coupling constant and asymmetry parameter are given by $C_Q = eQV_{33}/h$ and $\eta_Q = (V_{11} - V_{22})/V_{33}$, respectively. The sign of C_Q cannot be determined from the experimental ^{35}Cl spectra. [d]The chemical shift tensors are defined using the Herzfeld−Berger convention, in which the principal components are ordered $\delta_{11} \geq \delta_{22} \geq \delta_{33}$. The isotropic chemical shift, span, and skew are given by $\delta_{iso} = (\delta_{11} + \delta_{22} + \delta_{33})/3$, $\Omega = \delta_{11} - \delta_{33}$, and $\kappa = 3(\delta_{22} - \delta_{iso})/\Omega$, respectively. [e]The Euler angles α, β, and γ define the relative orientation of the EFG and magnetic shielding tensors using the $ZY'Z''$ convention for rotation, in which the principal values of the magnetic shielding tensor are ordered $\sigma_{11} \leq \sigma_{22} \leq \sigma_{33}$. The experimental angles derived from ssNake (which uses the $ZX'Z''$ convention) are adjusted to match the calculated values extracted by EFGShield according to the following operations: $\alpha = \gamma$(ssNake); $\beta = \beta$(ssNake); $\gamma = \alpha$(ssNake) + 90°. [f]This parameter has little to no effect on the simulated ^{35}Cl SSNMR pattern.

packed into 3.2 or 1.3 mm o.d. zirconia rotors and acquired under static and MAS conditions using a Bruker NEO spectrometer, an 89 mm bore Oxford magnet, and either a home-built 3.2 mm HXYD MAS probe or a home-built 1.3 mm HXY MAS probe (B_0 = 18.8 T, $\nu_0(^1H)$ = 800.13 MHz, and $\nu_0(^{35}Cl)$ = 78.36 MHz). Full details of the experimental parameters are provided in the Supporting Information (Tables S3−S9).

2.6.2. ^{13}C SSNMR Spectra. ^{13}C SSNMR spectra of all forms of X were acquired at 9.4 T using a $^1H \rightarrow ^{13}C$ variable-amplitude cross-polarization (VACP) MAS technique,[68−71] using SPINAL-64 ^{1}H decoupling with $\nu_2(^1H)$ = 50 kHz, a spinning rate of ν_{rot} = 11 or 12 kHz, a $\pi/2$ ^{1}H pulse width of 5.0 μs, optimized contact times between 0.7 and 0.9 ms, and an optimized recycle delay of 10 s. Spectra for the coformers were collected using a $\pi/2$ ^{1}H pulse width of 2.0 μs, optimized contact times between 1.0 and 1.7 ms, and a recycle delay of 250 s. Chemical shifts were referenced to TMS using the carbonyl carbon in ^{13}C-labeled α-glycine at $\delta_{iso}(^{13}C)$ = 176.5 ppm as a secondary reference.[72,73]

2.6.3. ^{35}Cl SSNMR Spectra. Static ^{35}Cl{^{1}H} SSNMR spectra were acquired using Hahn-echo,[74] CPMG,[75] or WURST-CPMG[76−79] pulse sequences with continuous wave (CW) ^{1}H decoupling at $\nu_2(^1H)$ = 25−35 kHz. ^{35}Cl{^{1}H} MAS SSNMR spectra (ν_{rot} = 16 or 30 kHz) were acquired using the Hahn-echo sequence, sometimes utilizing rotor-assisted population transfer (RAPT) *via* 64 μs WURST-80 pulses,[80,81] and a CW ^{1}H decoupling field of $\nu_2(^1H)$ = 25 or 55 kHz. Chemical shifts were referenced to NaCl(s) at δ_{iso} = 0.0 ppm. All spectra were processed and fit using the ssNake software package.[82] Uncertainties in quadrupolar and chemical shift parameters were estimated *via* bidirectional variation of the parameters, and visual comparison of various simulations overlaid with spectra. The reported Euler angles from ssNake, which describe the relative orientation of the magnetic shielding and EFG tensors, are converted from the $ZX'Z''$ convention for rotation to the $ZY'Z''$ convention, to facilitate comparison with calculated values (see Table 2 for details).[82,83]

2.7. Plane-Wave Density Functional Theory (DFT) Calculations. All plane-wave DFT calculations were performed using the CASTEP module within Materials Studio 2020.[84] The calculations employed the RPBE functional,[85] a plane-wave cutoff energy of 800 eV, and ZORA ultrasoft pseudopotentials generated on the fly.[86] Integrals over the Brillouin zone were sampled using a Monkhorst−Pack grid with a *k*-point spacing of 0.05 Å^{-1}.[87] Dispersion was implemented in the geometry optimizations using a modification of Grimme's two-body dispersion force field,[88] as discussed in previous work.[89−91] The SCF convergence threshold was 5×10^{-7} eV atom^{-1}. Geometry optimization and energy minimization used the low-memory BFGS algorithm.[92] Structural convergence was assessed using a maximum change in energy of 5×10^{-6} eV atom^{-1}, a maximum displacement of 5×10^{-4} Å atom^{-1}, and a maximum

https://doi.org/10.1021/acs.cgd.2c01539
Cryst. Growth Des. 2023, 23, 3412−3426

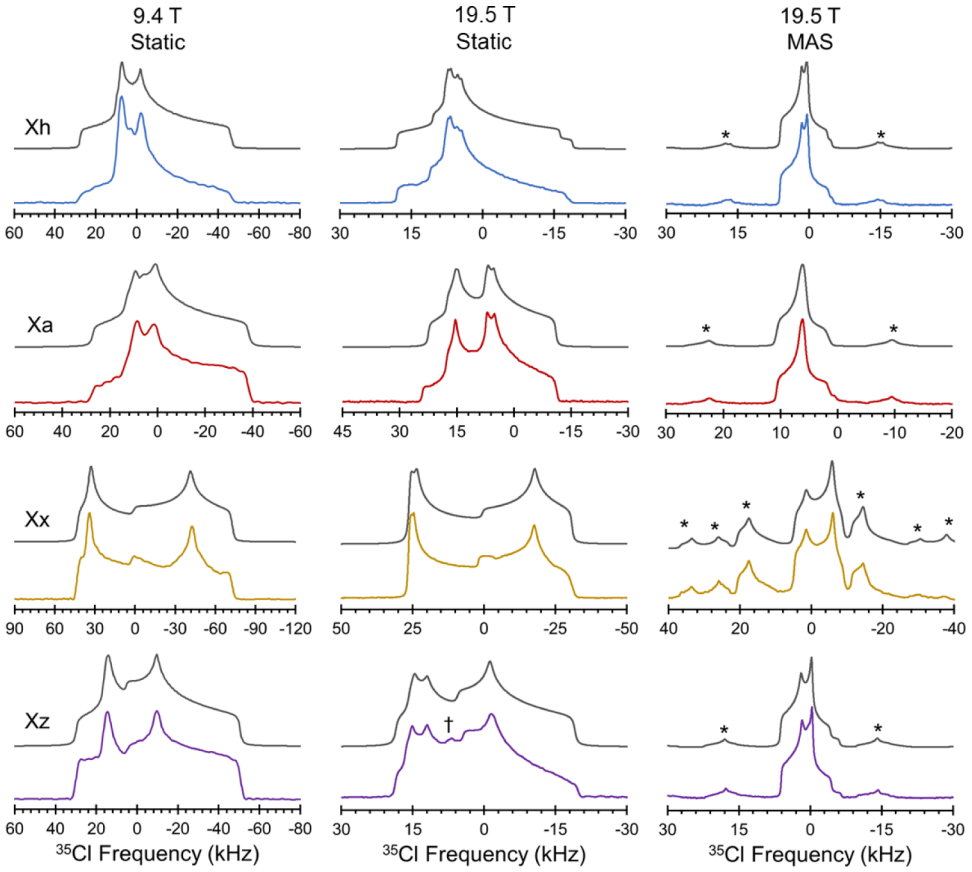

Figure 1. Experimental $^{35}Cl\{^{1}H\}$ SSNMR spectra of **Xh** (blue), **Xa** (red), **Xx** (orange), and **Xz** (purple), along with corresponding analytical simulations (black). Spectra at B_0 = 9.4 T were acquired under static conditions with the WURST-CPMG pulse sequence. Spectra at B_0 = 19.5 T were acquired under static and MAS (ν_{rot} = 16 kHz) conditions using the Hahn-echo pulse sequence. Spinning sidebands are indicated with asterisks (*). Impurity arising from **Xh** is denoted with a dagger (†).

Cartesian force of 10^{-2} eV Å^{-1}. Chlorine magnetic shielding tensors were computed using the GIPAW approach[93] and converted to the chemical shift scale relative to solid NaCl by setting the calculated magnetic shielding of NH_4Cl to $\delta_{iso}(^{35}Cl)$ = 120 ppm.[94] Euler angles, which use the $ZY'Z''$ convention for rotation, were extracted from the CASTEP output files using EFGShield 4.1.[83] The procedure for calculating ^{13}C chemical shifts uses both CASTEP and the Amsterdam Modelling Suite (AMS), as described in Supporting S1.

3. RESULTS AND DISCUSSION

3.1. Overview and General Observations. *3.1.1. Overview.* We discuss optimized conditions required for the successful synthesis and/or interconversion of four anhydrous polymorphs and one monohydrate of X; this includes a discussion of a novel polymorph, **Xy**, whose synthesis and structural characterization are presented here for the first time. In addition, we discuss the production and characterization of three novel cocrystals of X *via* ball milling. Ball milling conditions (frequency, number of ball bearings, and milling and ball bearing materials) and solvents were chosen to optimize for maximum yields for all preparations. PXRD, thermal analysis, and ^{13}C and ^{35}Cl SSNMR data, along with structural interpretations, are presented to confirm the identities of the products and potential impurities. Crystal structures from SCXRD are reported for the four novel solid forms, and the structure of **Xh** is redetermined.

Before proceeding to a discussion of each system, general observations on features from PXRD, and ^{13}C and ^{35}Cl SSNMR data are discussed. Then, detailed descriptions of the syntheses, thermal analysis, SCXRD, ^{13}C SSNMR, and ^{35}Cl SSNMR characterizations of four anhydrous polymorphs and one monohydrate of X are presented, followed by the three novel cocrystals of X. We discuss the refinement of the crystal structures of these eight forms of X using dispersion-corrected plane-wave DFT calculations (*i.e.*, DFT-D2*).[89−91] Finally, we present DFT calculations of ^{35}Cl EFG tensors and discuss their relationships with the local structural environments of the chloride ions, which may aid future attempts to predict structures of novel solid forms of X, or other APIs and associated cocrystals, in the absence of diffraction data.

3.1.2. Powder X-ray Diffraction. Prior to the synthesis of different solid forms of X and its cocrystals, PXRD patterns were acquired for all solid reagents. The PXRD patterns of different "as-received" samples of X reveal either **Xa**, **Xz**, or a mixture of **Xh** and **Xz** (Figure S1), based on comparisons to simulated PXRD patterns from the known crystal structures (this raised questions about the best starting point for developing an understanding of interconversions among the different solid forms, *vide infra*).[61] PXRD patterns of Bzc, Bza, and Mal (Figure S2) match well with those simulated from known SCXRD data.[59−61] The PXRD patterns of the cocrystals indicate pure products and do not reveal any evidence of starting materials (Figures S3−S5).

In part, PXRD data support the successful synthesis of the different solid forms of X and its cocrystals (*vide infra*). PXRD patterns of all previously reported solid forms of X match well with simulations and indicate samples of high crystallinity

https://doi.org/10.1021/acs.cgd.2c01539
Cryst. Growth Des. 2023, 23, 3412−3426

(Figure S6). For all novel solid forms of X, the absence of any obvious peaks arising from unreacted reagents (*i.e.*, educts) suggests the production of novel solid forms. After SCXRD data for the novel solid phases were obtained, the purities of the products of additional syntheses were verified through comparison of PXRD data with simulations based on the crystal structures (Figure S7).

Finally, because the samples were prepared over a period of several years, and in multiple locations with different atmospheric conditions, PXRD patterns were acquired prior to analysis by SSNMR, to provide an additional avenue for characterizing the materials and assessing their purities.

3.1.3. $^{1}H\rightarrow^{13}C$ SSNMR Spectra. ^{13}C CP/MAS spectra acquired at 9.4 or 14.1 T are useful for phase characterization, detection of impurities, and basic structural interpretation. The detection of impurity phases arising from incomplete transformations from the starting educt of X and/or coformers, or the interconversion between phases due to exposure to atmospheric conditions, provides a complementary method to PXRD for characterizing samples. Additionally, peak assignments can be made with the aid of DFT calculations (Tables S10 and S11), which can provide useful site-specific chemical interpretations (*vide infra*).

3.1.4. ^{35}Cl SSNMR Spectra. $^{35}Cl\{^{1}H\}$ MAS NMR spectra were acquired at 18.8 or 19.5 T to separate the central isotropic powder pattern from the spinning sidebands, allowing for the determination of the quadrupolar coupling constants, C_Q, asymmetry parameters, η_Q, and isotropic chemical shifts, δ_{iso}. Static $^{35}Cl\{^{1}H\}$ SSNMR spectra were collected at 9.4 T, and either 18.8 or 19.5 T, in order to deconvolute spectral contributions from the EFG and CS tensors, to refine the parameters obtained from MAS NMR spectra, and to extract the anisotropic CS parameters and Euler angles describing the relative orientation of the EFG and CS tensors (see Table 2 for a complete listing of all EFG and CS tensor parameters and conventions).

The $^{35}Cl\{^{1}H\}$ SSNMR spectra of all samples are typical of those of chloride ions in HCl salts of organic APIs (Figures 1−3). Most of the CT patterns are dominated by contributions from the SOQI, though the effects of chlorine CSA can be observed in the high-field spectra (N.B.: because of the MAS NMR spectra, the uncertainties in δ_{iso}, C_Q, and η_Q are small in comparison to those of the CS tensor parameters and Euler angles). The difference between each of the patterns is visually striking, with each having key discontinuities that arise from the unique EFG and CS tensors and their distinct relative orientations. In all cases, it is clear that these spectra correspond to very different chloride ion environments, even without recourse to simulations, meaning that the ^{35}Cl CT powder patterns function as useful spectral fingerprints for rapidly and reliably distinguishing solid forms. The $^{35}Cl\{^{1}H\}$ SSNMR spectra for all materials feature a number of CT patterns that are consistent with the number of crystallographically distinct chloride ions indicated by the crystal structures. ^{35}Cl SSNMR spectra are very useful for the detection of impurities, which are often not apparent in corresponding PXRD patterns. More details on the ^{35}Cl SSNMR spectra of each sample, the anisotropic NMR interaction parameters derived from these spectra, and their relationships to synthesis and structure, are discussed below.

3.2. Hydrate and Anhydrous Polymorphs. *3.2.1. Synthesis and Characterization.* There are five previously reported solid forms of X under ambient conditions: one monohydrate (**Xh**) and four anhydrous polymorphs (**Xa**, **Xx**, **Xz**, and **Xm**),[59,61] with reported preparations shown in Scheme 2. Form **Xh** can be produced from **Xa**, **Xx**, or **Xz** by slow recrystallization from water or placement in a hydration chamber. Conversely, form **Xh** can be heated at 100 °C for 2 days to produce **Xa**, or to 48−60 °C for 1 day to produce **Xx**. Interestingly, **Xz** and **Xm** are not reported to be formed in this manner; instead, **Xa** is converted to **Xz** through recrystallization from dry MeOH,[62,63] whereas **Xm** results from the desolvation of the DCM solvate of X (which is prepared by recrystallization of **Xa** from DCM).[63] Several studies have examined the relative stabilities of these solid forms, as well as the kinetics of their phase transitions. **Xh** is the most stable phase,[63] whereas the relative stabilities of the anhydrous polymorphs vary with temperature.[62] Of the anhydrous polymorphs, **Xz** is the most stable near RT, whereas **Xa** is the most stable above 48 °C, and **Xx** is the least stable across this temperature range. The transformation of **Xx** to **Xa** has been explored in some detail,[95] as has the dehydration of **Xh** to produce **Xx** or **Xa**.[96] Factors that are known to influence the kinetics of phase transformations include temperature, pressure, humidity, and particle size distribution of the educt.

We found commercial samples of as-received X to contain different solid forms (*i.e.*, **Xa**, **Xz**, or a mixture of **Xz** and **Xh**, Figure S1). This led us to carefully investigate the rigid sets of synthetic conditions to reliably produce a single solid form. We found that no matter what the initial starting form is, we can reliably produce **Xh** *via* (i) recrystallization from distilled water by slow evaporation;[62] (ii) storing the sample in a hydration chamber for *ca.* 2 days;[63] or (iii) ball milling the sample in the presence of 0.5 mol equiv of water for 30 min (this latter method has not been reported to date). Additionally, we were able to grow single crystals of **Xh** by slow evaporation from distilled water; from these, we redetermined the structure *via* SCXRD (*vide infra*).

Once we established the robust production of pure **Xh**, we initiated a series of experiments aimed at producing the other solid forms. First, attempts to produce the anhydrous polymorphs **Xa** and **Xx** by dehydration of **Xh** under vacuum using previously reported procedures were successful, with complete dehydration observed at 100 and 50 °C, respectively, after 3 days.[96] Attempts to prepare **Xa** and **Xx** by ball milling under ambient conditions were unsuccessful, as they only seem to form under conditions of low pressure (N.B.: now that we could reliably produce the stable forms **Xa** and **Xx**, we also used these as educts for the synthesis of new solid forms). Second, we found that **Xz**, which can be prepared *via* recrystallization of **Xa** from MeOH,[62] could also be produced by LAG of **Xa**, **Xx**, **Xz**, or **Xh** with two 5 mm stainless steel or 3 Å 4−8 mesh molecular sieves in solvents such as MeOH, EtOH, or DMF. The molecular sieves were found to be crucial for trapping water and preventing the persistence and/or formation of **Xh** (or other potential hydrated forms) within the Teflon-based milling containers. Third, we attempted to make **Xm**, which was reported as being prepared by a two-step process involving (i) recrystallization of **Xa** from DCM to yield a DCM solvate of X and (ii) subsequent desolvation over one day at low RH to yield **Xm**;[63] our attempts at duplicating this result were unsuccessful. However, after numerous trials involving LAG with any form of X, two molecular sieves, and MeCN, we produced a novel anhydrous polymorph, **Xy**. We note that milling **Xa** with MeCN and two stainless steel ball bearings, rather than molecular sieves, led to incomplete

https://doi.org/10.1021/acs.cgd.2c01539
Cryst. Growth Des. 2023, 23, 3412−3426

Scheme 3. Reaction Pathways for Interconversion of the Polymorphs and Hydrate of Xylazine HCl (X)[a]

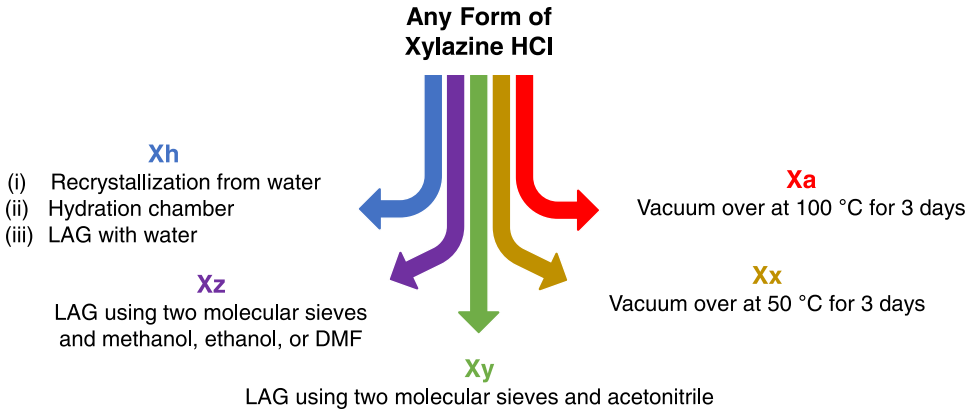

[a]The pathways in blue, purple, green, orange, and red correspond to the synthesis of xylazine HCl monohydrate (**Xh**), form Z (**Xz**), form Y (**Xy**), form X (**Xx**), and form A (**Xa**), respectively.

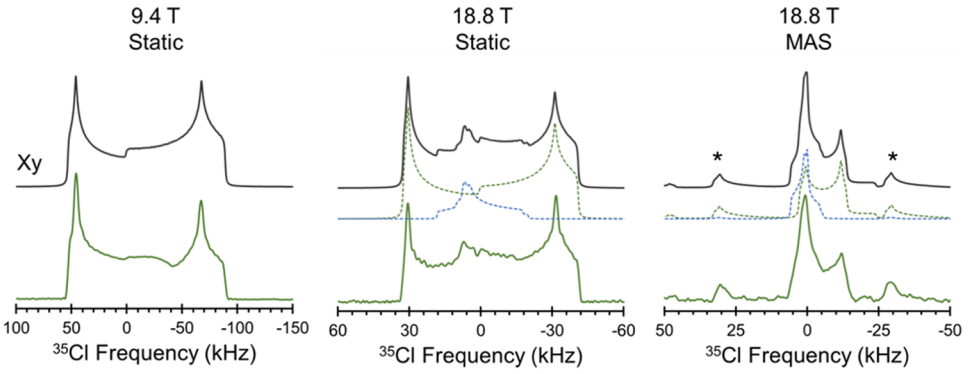

Figure 2. Experimental (green) and simulated (black) $^{35}Cl\{^{1}H\}$ static and MAS SSNMR spectra of novel anhydrous form **Xy** acquired at 9.4 and 18.8 T. Static and MAS spectra reveal the presence of an impurity, **Xh**, from hydration, indicated in the simulation in light blue. Spinning sidebands are indicated with asterisks (*).

conversion to **Xy**, resulting in a mixture of polymorphs easily observable in ^{35}Cl SSNMR (Figure S15).

Previous reports of interconversions between solid forms of X, as well as the novel LAG experiments described above, convinced us to further explore the landscape of possible synthetic conditions. Therefore, we took each of the anhydrous solid forms and subjected them to the synthetic conditions described above (see Scheme 3). We found that in every case, it was possible to produce each solid form in high yields (*i.e.*, with little or no impurity detected by PXRD), provided that the synthetic conditions were rigorously adhered to. Hence, it appears that the formation of each solid form of X is independent of the educt and dependent solely on the synthetic conditions.

3.2.2. Thermal Analysis. DSC thermograms and TGA curves for the monohydrate and anhydrous polymorphs of X are found in Figures S8 and S9. The DSC thermograms for **Xa** and **Xy** feature a single endothermic peak with no loss of mass observed in the corresponding TGA curves, which likely corresponds to the melting of the solid. In contrast, the DSC thermograms for **Xx** and **Xz** feature multiple endothermic events. Of these, the events in the range of *ca.* 100−110 °C likely correspond to the disproportionation of the HCl salts (which is suggested by the loss of mass in the TGA curves). A second event corresponding to the melting of freebase X is observed at *ca.* 140 °C.[97] Possible solvent loss is also observed. Finally, the DSC thermogram for **Xh** exhibits two endothermic events, neither of which coincide with mass loss in the TGA curve, suggesting the formation of a new phase at *ca.* 80−90 °C, before melting. Previous work has illustrated that the dehydration of **Xh** yields either **Xa** or **Xx**, depending on conditions such as temperature, pressure, and humidity;[63] our results indicate a single melting endotherm, illustrating that dehydration of **Xh** yields **Xa** uniquely, under these experimental conditions.

3.2.3. Crystal Structures. The SCXRD structures of **Xa**, **Xx**, **Xz**, and **Xh** have been reported previously.[59] We report a new crystal structure for the monohydrate **Xh** (Figure S16), which differs from the previously reported structure acquired at different temperatures and pressures,[59,61] as well as that of a novel anhydrous polymorph, **Xy** (Figure S17). The previously reported anhydrous polymorphs and monohydrate of X all belong to the monoclinic $P2_1/c$ space group (no. 14, $Z = 4$, $Z' = 1$), whereas the novel form **Xy** crystallizes in the hexagonal space group $P6_1$ (no. 169, $Z = 6$, $Z' = 1$). It is also noteworthy that the molecular-level structure of the xylazine molecule within **Xy** differs significantly from that of all previously reported solid forms of X; this is most clearly reflected in the N3−C4−N5−C6 torsional angle, which is *ca.* 5° in **Xy**, but closer to *ca.* 175° for the other forms.

3.2.4. $^{1}H\rightarrow^{13}C$ SSNMR Spectra. The $^{1}H\rightarrow^{13}C\{^{1}H\}$ VACP/MAS spectra of the anhydrous polymorphs and monohydrate of X have common groupings of chemical shifts in regions between *ca.* 10−50 and *ca.* 120−170 ppm (Figure S10). Slight

https://doi.org/10.1021/acs.cgd.2c01539
Cryst. Growth Des. 2023, 23, 3412−3426

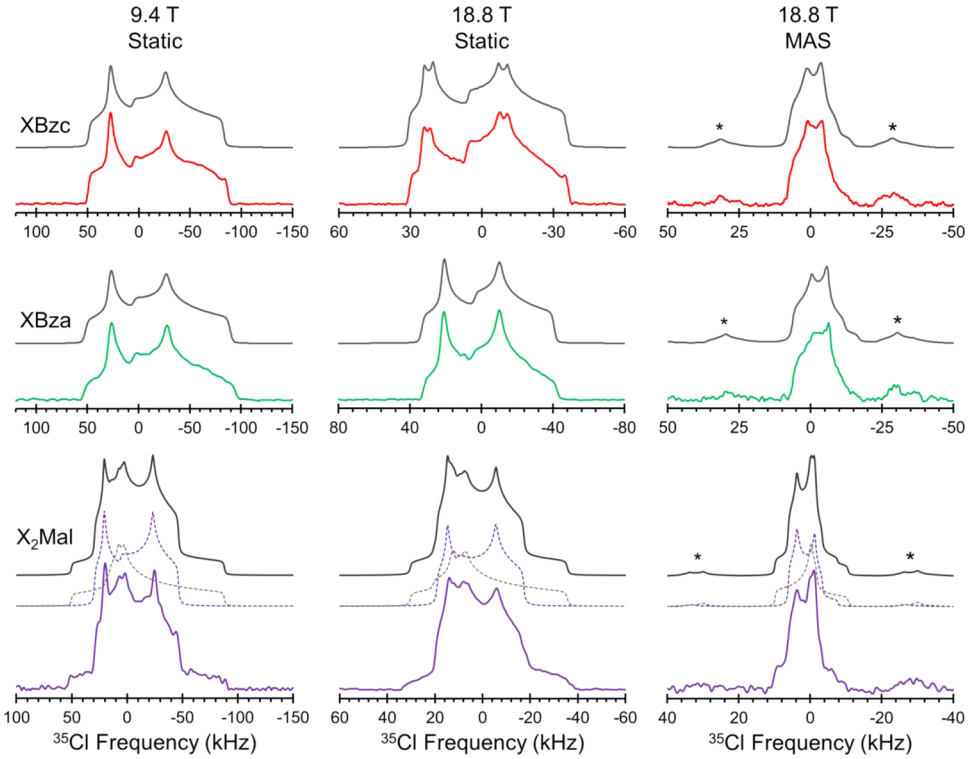

Figure 3. Experimental $^{35}Cl\{^{1}H\}$ SSNMR spectra of **XBzc** (red), **XBza** (green), and **X_2Mal** (purple) along with the corresponding analytical simulations (black). Spectra at B_0 = 9.4 T under static conditions were acquired with the WURST-CPMG pulse sequence. Spectra at B_0 = 18.8 T under static and MAS (ν_{rot} = 30 kHz) conditions were acquired using the QCPMG and RAPT-echo pulse sequences, respectively. Spinning sidebands are indicated with asterisks (*).

differences in chemical shifts among spectra are expected for the distinct polymorphs and hydrated phases. In each case, several of the peaks overlap (especially in the methyl and aromatic regions), preventing the determination of the chemical shifts for all twelve carbon atoms within the xylazine molecule and concomitant crystal lattice. Furthermore, the spectra of **Xa**, **Xx**, and **Xy** all feature additional peaks that we attribute to the presence of impurity phases of X. In the cases of **Xa**, the impurity corresponds only to **Xz**, whereas for **Xa** and **Xy**, the impurities are attributable to both **Xz** and **Xh**. We note that these impurity phases were not always detected beforehand by PXRD (*i.e.*, no impurity was detected in the PXRD pattern for **Xa**, whereas the pattern for **Xx** indicated only the **Xh** impurity); this suggests that the samples sometimes contain impurity phases that are below the limit of detection of PXRD due to incomplete transformation from the educt form of X, as part of an ongoing transformation process due to exposure to atmospheric water, or even that the transformations between solid forms of X could be facilitated *in situ* by frictional heating during magic-angle spinning. DFT calculations of the ^{13}C chemical shifts are illustrated in Figure S11; however, the authors stress that peak assignments made on the basis of isotropic chemical shifts alone often result in errors, but can be facilitated through various 2D methods.[98]

3.2.5. ^{35}Cl SSNMR Spectra. $^{35}Cl\{^{1}H\}$ CT patterns acquired at 9.4 T range in breadth from *ca.* 70−150 kHz, while those acquired at 18.8 or 19.5 T are narrower for both static and MAS experiments (*ca.* 33−78 and *ca.* 22−26 kHz, respectively) due to the inverse field dependence of the SOQI on pattern breadth (Figures 1 and 2). These pattern breadths are typical for CT powder patterns of chloride ions in HCl salts.[30,31,36] Simulations of the $^{35}Cl\{^{1}H\}$ spectra acquired at multiple fields for all forms of X allow for the determination of the EFG and CS tensor parameters, with the magnitudes of C_Q ranging from 3.29 to 6.15 MHz (Table 2) and **Xy** having the largest.

^{35}Cl SSNMR spectra are very useful for the detection of impurities, which were only detected in the spectra of **Xz** and **Xy**. The static spectrum of **Xz** acquired at 19.5 T reveals the presence of a small quantity of **Xh** that arises from the uptake of moisture (Figure 1). This is supported by the ^{35}Cl static pattern of **Xh** that has a sharp set of discontinuities at the same position. Evidence of an impurity is also observed in both the ^{35}Cl static and MAS spectra of **Xy** acquired at 18.8 T (Figure 2), which indicates that the sample converts to **Xh** over time (samples were shipped from Windsor to Tallahassee in tightly sealed containers; nonetheless, some interconversion occurred, perhaps due to the accumulation of trace water on the glass surfaces). Overlays of simulated static and MAS spectra of **Xy** and **Xh** clearly indicate the presence of **Xh** as a minor component; the static spectrum is more reliable for deconvolution and measurement of integrated intensities,[99] with patterns corresponding to **Xy** and **Xh** having a ratio of integrated intensities of 6.5:1.

3.3. Cocrystals. *3.3.1. Mechanochemical Synthesis.* We synthesized three novel cocrystals mechanochemically by NG of X with coformers Bzc, Bza, and Mal, in the appropriate stoichiometric ratios, yielding cocrystals **XBzc**, **XBza**, and **X_2Mal**, respectively. We attempted each synthesis with varying solid forms of **X** used in the ball milling reactions (**Xa**, **Xz**, **Xh**, and **Xx**), and each led to the same product. Neat grinding yielded pure white, crystalline, powdered products, which were distinguished from the mixtures of educts *via* a combination of PXRD (Figures S3−S5), ^{13}C SSNMR (Figure S15), and ^{35}Cl

https://doi.org/10.1021/acs.cgd.2c01539
Cryst. Growth Des. 2023, 23, 3412−3426

Table 3. List of H···Cl^- Contacts and Calculated ^{35}Cl SSNMR Parameters for Xylazine HCl Polymorphs, Hydrates, and Cocrystals

	contact type[a]	H···Cl^- distance[b] (Å)	X···Cl^- distance[c]	X−H···Cl^- angle[d] (deg.)	C_Q (MHz)	η_Q	δ_{iso} (ppm)
Xh	HOH···Cl^-	2.178	3.111	177.9	3.80	0.53	80
	HOH···Cl^-	2.211	3.121	165.2			
	RR′NH···Cl^-	2.253	3.211	167.2			
Xa	RR′NH^+···Cl^-	2.155	3.090	159.3	−3.56	0.63	141
	RR′NH···Cl^-	2.237	3.147	154.7			
Xx	RR′NH···Cl^-	2.161	3.131	168.4	−4.72	0.50	76
	RR′NH^+···Cl^-	2.354	3.186	143.1			
Xy	RR′NH···Cl^-	2.097	3.081	177.6	−6.08	0.17	95
	RR′NH^+···Cl^-	2.245	3.091	144.6			
Xz	RR′NH^+···Cl^-	2.138	3.083	161.0	−3.40	0.99	87
	RR′NH···Cl^-	2.209	3.121	154.4			
XBzc	ROOH···Cl^-	2.052	2.999	172.3	−5.22	0.68	112
	RR′NH···Cl^-	2.102	3.076	171.1			
XBza	RR′NH···Cl^-	2.176	3.135	165.2	−5.06	0.60	89
	RNH_2···Cl^-	2.390	3.352	174.4			
	RNH_2···Cl^-	2.405	3.342	164.9			
X_2Mal (Cl1)	ROOH···Cl^-	2.040	2.988	171.0	3.98	0.35	109
	RR′NH···Cl^-	2.118	3.083	168.5			
	RR′NH^+···Cl^-	2.285	3.159	149.2			
X_2Mal (Cl2)	ROOH···Cl^-	2.050	3.000	175.7	4.93	0.91	144
	RR′NH···Cl^-	2.149	3.092	161.8			
	RR′NH^+···Cl^-	2.406	3.275	149.3			

[a]Indicates the functional group involved in the H···Cl^- bond (*i.e.*, RR′NH_2^+···Cl^- signifies a positively charged secondary amine contact, RR′NH_2···Cl^- signifies a neutral secondary amine contact, and HOH···Cl^- indicates a water molecule contact). [b]The shortest H···Cl^- hydrogen bonds (<2.6 Å), as determined *via* energy minimization and geometry optimization with RPBE-D2* DFT plane-wave calculations. [c]The distance between the chloride ion and the hydrogen-bond donor atom (X = N, O). [d]Angle between the hydrogen-bond donor atom (X = N, O), the hydrogen atom, and the chloride ion.

SSNMR (Figure 3). Mechanochemical syntheses using other coformers were also attempted; however, these ball milling experiments resulted in physical mixtures of educts rather than new cocrystals.

3.3.2. Thermal Analysis. DSC thermograms and TGA curves for the cocrystals of X are found in Figures S12 and S13. The DSC thermograms for **XBzc** and **X_2Mal** feature single endothermic peaks, likely corresponding to the melting of the cocrystals, with subsequent mass loss in the TGA plot for **X_2Mal** attributable to the decomposition of malonic acid at 135 °C. The DSC thermogram for **XBza** features three endothermic peaks, likely corresponding to the decomposition of the cocrystal and the release of HCl, followed by the melting of benzamide (*ca.* 125 °C) and freebase xylazine (*ca.* 140 °C).[97]

3.3.3. Crystal Structures. Following the identification of unique products by PXRD and SSNMR, a small portion of each product was dissolved and recrystallized by slow solvent evaporation, yielding crystals suitable for analysis by SCXRD (Figures S19−S21). Predicted powder patterns based on structures determined from SCXRD data matched initial experimental PXRD data, confirming the formation of the cocrystals **XBzc**, **XBza**, and **X_2Mal** upon initial grinding. These structures were solved in the monoclinic $C2/c$ (no. 15, $Z = 8$, $Z' = 1$), triclinic $P\bar{1}$ (no. 2, $Z = 2$, $Z' = 1$), and orthorhombic $P2_12_12_1$ (no. 19, $Z = 4$, $Z' = 1$) space groups, respectively. The asymmetric units of **XBzc** and **XBza** feature a single API molecule, one crystallographically distinct chloride ion, and one coformer molecule. The crystal structure of **X_2Mal** features two crystallographically distinct chloride ions. Crystallographic parameters and additional details of all single-crystal structures are found in Tables S12 and S13.

3.3.4. $^1H \rightarrow ^{13}C$ SSNMR Spectra. ^{13}C CP/MAS spectra for the cocrystals have similar arrays of peak groupings as observed for the other solid forms of X (Figure S15), with the exception of the shifts corresponding to the coformer molecules. Peaks corresponding to the carboxylic acid or amide carbon atoms of the coformers appear at *ca.* 175−180 ppm, with distinct shifts for each cocrystal. This suggests that there is no transfer of protons between the charged molecules of X and the coformers. The large number of overlapping peaks observed in the spectrum of **X_2Mal** is consistent with a crystal structure that has two crystallographically distinct molecules of X. None of the spectra show evidence of unreacted educts, although there is some indication of an impurity phase in the spectrum of **X_2Mal**. As with the case of the monohydrate and anhydrous polymorphs of X, DFT calculations of ^{13}C chemical shifts are provided in Figure S16.

3.3.5. ^{35}Cl SSNMR Spectra. The ^{35}Cl NMR spectra of the cocrystals (Figure 3) reveal CT patterns that are distinct from those of all other forms of X, as well as one another, and do not indicate the presence of educts or impurities. The ^{35}Cl NMR spectra of **X_2Mal** reveal two overlapping patterns, indicating the presence of two crystallographically distinct chlorine sites (*i.e.*, Cl1 and Cl2). The two patterns can be assigned unambiguously *via* the use of DFT calculations of the ^{35}Cl EFG tensors, in which Cl1 corresponds to the narrow CT pattern ($C_Q = 4.28$; $\eta_Q = 0.30$), and Cl2 corresponds to the broad CT pattern ($C_Q = 4.73$; $\eta_Q = 0.97$). For the high-field MAS spectrum, the integrated intensity of Cl1 is slightly greater than that of Cl2, with a ratio of 1.1:1.0 (N.B. the

https://doi.org/10.1021/acs.cgd.2c01539
Cryst. Growth Des. 2023, 23, 3412−3426

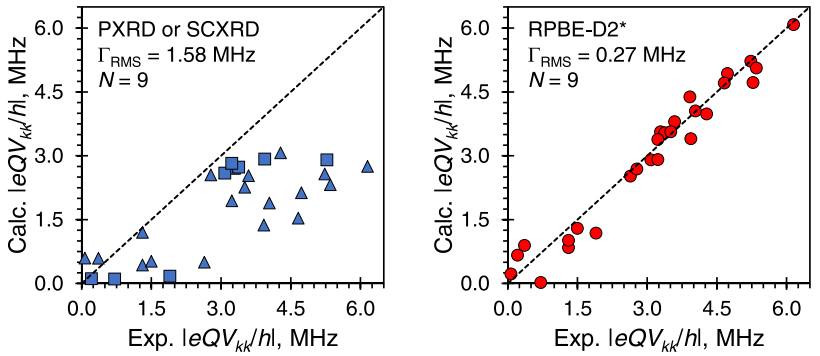

Figure 4. Relationships between principal components of the ^{35}Cl EFG tensors that have been measured experimentally and determined with DFT-D2* calculations. Results are shown for unrefined structures obtained by X-ray diffraction (left), as well as structures refined at the RPBE-D2* level (right). Dotted lines represent perfect agreement between calculated and experimental values. Γ_{RMS} and N denote the root-mean-square EFG distance and the number of chloride ion sites, respectively.

spectrum was acquired using a RAPT-echo sequence with CT-selective pulses, which results in uniform nutations of individual isochromats, ensuring that integrated intensities can be regarded as quantitative. Additionally, since values of T_2^{eff} for chloride ions are typically on the order of 2−20 ms, the interpulse delay of 10 μs used here has limited impact on integrated intensities).

3.4. Plane-Wave DFT Calculations. Dispersion-corrected plane-wave DFT-D2* calculations can be used to obtain geometry-optimized structures for periodic systems, as well as to calculate NMR interaction tensors based on experimentally determined or computationally refined crystal structures (Table 3; a comparable analysis for the unrefined structures is provided in Table S14). Herein, the relationships between experimentally measured ^{35}Cl EFG tensors, which are very sensitive to chloride ion hydrogen-bonding arrangements, are used as metrics to assess the validity of structures. Calculations are performed on models based on PXRD or SCXRD structures, as well as model structures that have been refined with dispersion-corrected DFT-D2* calculations. The DFT-D2* calculations have been parameterized in previous work from our laboratory to provide accurate placements of hydrogen atoms, based on a comparison of experimentally measured and theoretically derived EFG and CS tensors for several nuclides.[89−91] Since there are relatively straightforward relationships between the local structures of the chloride ions and the ^{35}Cl EFG tensor parameters and orientations (*vide infra*),[30,31,36,54] we explore this further for all of the systems described herein.

The experimental ^{35}Cl EFG and CS tensors are compared with those obtained from plane-wave DFT calculations using model structures based on experimentally determined structures (SCXRD or Rietveld refinement of PXRD data), and DFT-D2* refinements involving the repositioning of all atoms within a fixed unit cell (Table S15).[89−91] The improved quality of each crystal structure following geometry optimization at the RPBE-D2* level is indicated by the following criteria: (i) the reduction of the static lattice energies, (ii) the reduction of the RMS Cartesian forces on all atoms; and (iii) the reduction of the ^{35}Cl EFG distances, Γ_{EFG}, for each chloride ion. Comparison of the experimental and calculated ^{35}Cl EFG tensors (Figure 4) for the XRD-derived structures reveals very poor agreement, with an RMS Γ_{EFG} of 1.58 MHz for the nine chloride ions, whereas improved agreement is observed for the refined structures, with an RMS Γ_{EFG} of 0.27 MHz. Calculation on our refined crystal structure of **Xh** results in excellent agreement with experiment (Γ_{EFG} = 0.26 MHz), whereas calculations on five previously reported structures do not,[60,61] even though all geometry-optimized structures of **Xh** result in nearly identical static lattice energies (Table S16). The agreement between experimental and calculated chlorine CS tensors is more ambiguous, due to the fact that the CS tensor parameters and Euler angles are extracted from spectra dominated by contributions from the SOQI, and are therefore associated with higher uncertainties; these parameters are not discussed further.

Thermal effects on calculated ^{35}Cl EFG tensors have been discussed previously.[91] In general, the effect of small lattice expansions/contractions associated with changes in temperature have only small effects on calculated EFG tensors. For example, the calculated values of C_Q for the chloride ion in L-histidine HCl·H_2O differ by only 120 kHz for DFT-D2* geometry-optimized structural models based on SCXRD structures obtained at 298 and 100 K. However, in rare instances, motions of highly mobile moieties, such as NH_4^+ ions, can impact both calculated and experimental EFG tensors; in such cases, these effects can be modeled using *ab initio* molecular dynamics.[54]

The types and arrangements of hydrogen bonds around chloride ions are correlated to the ^{35}Cl EFG tensors (Table 3).[30,31,36,54,57] Hydrogen bonds with the largest influence on the ^{35}Cl EFG tensors are those in which the H···Cl^- distance is less than *ca.* 2.2 Å, which we define here as short contacts, whereas all interactions up to *ca.* 2.6 Å are referred to as long contacts.[100−102] When systems have a single short contact, DFT calculations invariably show that the sign of C_Q is negative (*i.e.*, the sign of V_{33} is positive, since $Q(^{35}Cl)$ = −8.165 fm^2),[103] and the largest principal component of the EFG tensor, V_{33}, is oriented in the general direction of the short contact. When systems have two short contacts, calculations indicate that the sign of C_Q is positive, and the negative principal component V_{33} is oriented approximately perpendicular to the plane formed by the two short contacts (*i.e.*, EFGs are positive in the directions of the two short contacts). However, in situations in which the two short contacts are aligned in a linear (or nearly linear) spatial arrangement, V_{33} is directed along the hydrogen-bonding axes, and the magnitude of C_Q is predicted to be negative.[38] In contrast, for systems that do not feature short contacts (*i.e.*, all hydrogen-bonding distances are greater than *ca.* 2.2 Å), the

https://doi.org/10.1021/acs.cgd.2c01539
Cryst. Growth Des. 2023, 23, 3412−3426

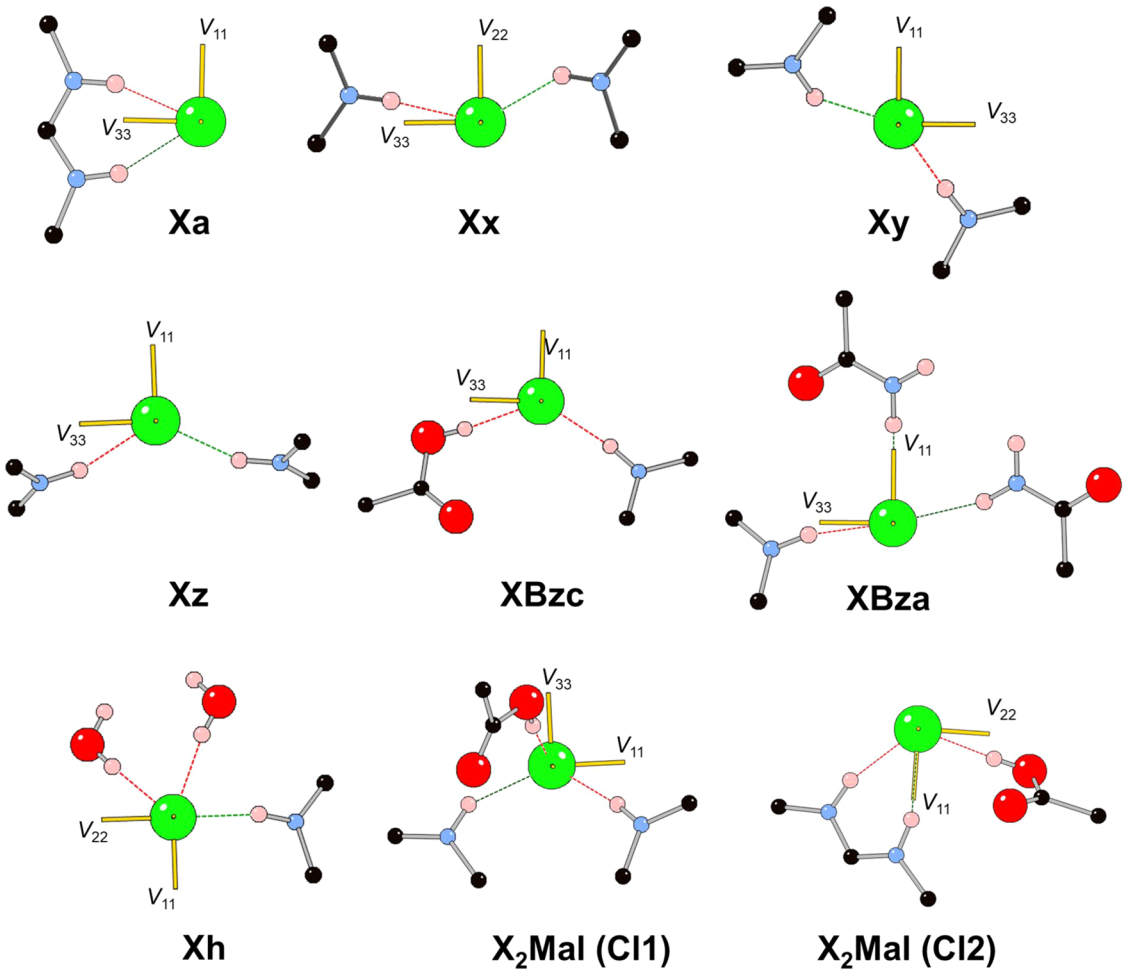

Figure 5. ^{35}Cl EFG tensor orientations for the different forms of X. The short (<2.2 Å) H···Cl contacts are shown in red. Hydrogen bonds (2.2−2.6 Å) are shown in green. Yellow vectors represent the orientations of the principal components of the EFG tensor (V_{11}, V_{22}, and V_{33}), where one vector is oriented perpendicular to the page.

relationships between EFG tensors and molecular-level structure are more complicated and vary from system to system, and generally have C_Q values of small magnitude.[31,36] As such, it is of interest to explore the relationships between the EFG tensor parameters, tensor orientations, and the chloride ion environments for the solid forms of X, as such information may be useful in future NMR crystallographic investigations of novel forms of APIs without crystal structures.

The calculated ^{35}Cl EFG tensor orientations for the refined structures of the solid forms of X are shown in Figure 5 (N.B.: the EFG tensor is centrosymmetric; however, we have chosen to use three yellow vectors to simplify the diagrams). For the four anhydrous polymorphs of X, the chloride ion resides in an environment featuring a single short contact and one additional long contact. In each case, calculations show that the value of C_Q is negative. **Xa**, **Xx**, and **Xz** feature an N3−C4−N5−C6 torsion angle near 180°, and V_{33} resides within the plane formed by the short and long contacts due to the spatial proximity of these two hydrogen-bond donating sites. In contrast, **Xy** features a torsion angle near 0°, and V_{33} is oriented in the direction of the short contact. Similarly, for **XBzc** and **XBza**, DFT calculations show that the value of C_Q is negative and V_{33} is oriented in the direction of the shortest contact, even when a second short contact is present, as is the case for **XBzc**. In contrast, the structure of **Xh** features two short contacts with water molecules, and calculations show that the sign of C_Q is positive, with V_{33} oriented approximately perpendicular to the plane formed by the chloride ion and the two short contacts. Calculations on the two chloride ions in **X_2Mal** also show that their values of C_Q are positive, and V_{33} components are oriented approximately perpendicular to the plane formed by the chloride ion and the two short contacts in each case.

In summary, the orientations of the ^{35}Cl EFG tensors are largely consistent with our previous observations on organic chloride salts. It is expected that this expanding body of data will be useful for gaining insight into crystal structures in the absence of structural data obtained from diffraction studies, and may even serve as the groundwork for future applications in NMR-guided crystal structure prediction, involving the EFG tensors as a primary metric, and possibly even artificial intelligence and/or machine learning, as has been recently explored with chemical shifts.[104−106]

4. CONCLUSIONS

We have determined optimized experimental conditions for synthesizing three previously reported anhydrous polymorphs, a monohydrate, and a novel anhydrous polymorph of xylazine HCl, as well as three new cocrystals with X as a component and carboxylic acids and an amide as coformers, all with high

https://doi.org/10.1021/acs.cgd.2c01539
Cryst. Growth Des. 2023, 23, 3412−3426

yields and rapidity. We characterized the microcrystalline samples with thermal analysis, PXRD, and multinuclear SSNMR spectroscopy, and determined crystal structures for the novel anhydrous polymorph, the hydrate, and three new pharmaceutical cocrystals. Additionally, dispersion-corrected plane-wave DFT-D2* calculations were used to obtain refined crystal structures, from which ^{35}Cl EFG tensors were computed and found to agree with experiment. The combination of ^{35}Cl SSNMR, PXRD, and quantum chemical calculations is invaluable for spectral fingerprinting, examining interconversion of polymorphs and hydrates, optimizing synthetic protocols, making structural assignments, and exploring the relationships between the local chloride ion environments and the ^{35}Cl EFG tensors. These combined methodologies should prove useful for future optimizations of mechanochemical syntheses of both polymorphs and cocrystals, perhaps even allowing for the rational design of new solid forms and aiding in *de novo* NMR crystallographic crystal structure prediction.

■ ASSOCIATED CONTENT

Supporting Information

The Supporting Information is available free of charge at https://pubs.acs.org/doi/10.1021/acs.cgd.2c01539.

Synthetic conditions; NMR acquisition parameters; summary of computational results; crystallographic information; PXRD; thermal analysis; and additional SSNMR spectra (PDF)

Accession Codes

CCDC 2214351−2214355 contain the supplementary crystallographic data for this paper. These data can be obtained free of charge via www.ccdc.cam.ac.uk/data_request/cif, or by emailing data_request@ccdc.cam.ac.uk, or by contacting The Cambridge Crystallographic Data Centre, 12 Union Road, Cambridge CB2 1EZ, UK; fax: +44 1223 336033.

■ AUTHOR INFORMATION

Corresponding Author

Robert W. Schurko − *Department of Chemistry & Biochemistry, Florida State University, Tallahassee, Florida 32306, United States; National High Magnetic Field Laboratory, Tallahassee, Florida 32310, United States;* orcid.org/0000-0002-5093-400X; Email: rschurko@fsu.edu

Authors

Louae M. Abdulla − *Department of Chemistry & Biochemistry, University of Windsor, Windsor, Ontario N9B 3P4, Canada*

Austin A. Peach − *Department of Chemistry & Biochemistry, Florida State University, Tallahassee, Florida 32306, United States; National High Magnetic Field Laboratory, Tallahassee, Florida 32310, United States*

Sean T. Holmes − *Department of Chemistry & Biochemistry, Florida State University, Tallahassee, Florida 32306, United States; National High Magnetic Field Laboratory, Tallahassee, Florida 32310, United States*

Zachary T. Dowdell − *Department of Chemistry & Biochemistry, Florida State University, Tallahassee, Florida 32306, United States; National High Magnetic Field Laboratory, Tallahassee, Florida 32310, United States*

Lara K. Watanabe − *Department of Chemistry & Biochemistry, University of Windsor, Windsor, Ontario N9B 3P4, Canada;* orcid.org/0000-0002-0327-5611

Emilia M. Iacobelli − *Department of Chemistry & Biochemistry, University of Windsor, Windsor, Ontario N9B 3P4, Canada*

David A. Hirsh − *Department of Chemistry & Biochemistry, University of Windsor, Windsor, Ontario N9B 3P4, Canada;* Present Address: Boehringer Ingelheim Pharmaceuticals, Inc., Ridgefield, Connecticut 06877, United States

Jeremy M. Rawson − *Department of Chemistry & Biochemistry, University of Windsor, Windsor, Ontario N9B 3P4, Canada;* orcid.org/0000-0003-0480-5386

Complete contact information is available at: https://pubs.acs.org/10.1021/acs.cgd.2c01539

Author Contributions

‖L.M.A., A.A.P., and S.T.H. contributed equally

Author Contributions

L.M.A., A.A.P., and S.T.H. made equal contributions to this manuscript. L.M.A. was responsible for the majority of sample preparations and initial manuscript drafts, A.A.P. was responsible for the design of synthetic procedures and characterization of products, and S.T.H. was responsible for first-principles calculations and final manuscript drafts. All three contributed to sample characterization using solid-state NMR, PXRD, and other methods. Z.T.D. assisted with refining mechanochemical syntheses and obtaining ^{13}C CP/MAS spectra. L.K.W. and J.M.R. were responsible for single-crystal XRD experiments and structure determination. E.M.I. and D.A.H. prepared some preliminary samples and collected SSNMR and PXRD data for them. L.M.A., A.A.P., S.T.H., J.M.R., and R.W.S. made significant contributions to the writing and editing of this manuscript

Notes

The authors declare no competing financial interest.

■ ACKNOWLEDGMENTS

The authors thank Genentech, the Florida State University, and the National High Magnetic Field Laboratory for funding this research. The National High Magnetic Field Laboratory was supported by the National Science Foundation through NSF/DMR-1644779 and the State of Florida. The authors also thank the Natural Sciences and Engineering Research Council of Canada (NSERC Discovery grants 2016-06642 and 2020-04627 for R.W.S. and J.M.R., respectively), the Canadian Foundation for Innovation, the Ontario Innovation Trust, the Ontario Research Fund, and the University of Windsor for supporting the initial stages of this project. A portion of this research used resources provided by the X-ray Crystallography Center at the FSU Department of Chemistry and Biochemistry. The authors also acknowledge use of the SSNMR and SCXRD facilities at the University of Windsor, supported by the Canadian Foundation for Innovation, Ontario Innovation Trust, and the University of Windsor.

■ REFERENCES

(1) Datta, S.; Grant, D. J. W. Crystal structures of drugs: advances in determination, prediction and engineering. *Nat. Rev. Drug Discovery* **2004**, *3*, 42−57.

(2) Healy, A. M.; Worku, Z. A.; Kumar, D.; Madi, A. M. Pharmaceutical solvates, hydrates and amorphous forms: A special emphasis on cocrystals. *Adv. Drug Delivery Rev.* **2017**, *117*, 25−46.
(3) Pindelska, E.; Sokal, A.; Kolodziejski, W. Pharmaceutical cocrystals, salts and polymorphs: advanced characterization techniques. *Adv. Drug Delivery Rev.* **2017**, *117*, 111−146.
(4) Karpinski, P. H. Polymorphism of active pharmaceutical ingredients. *Chem. Eng. Technol.* **2006**, *29*, 233−237.
(5) Khankari, R. K.; Grant, D. J. W. Pharmaceutical hydrates. *Thermochim. Acta* **1995**, *248*, 61−79.
(6) Byrn, S. R.; Zografi, G.; Chen, X. Solvates and Hydrates. In *Solid State Properties of Pharmaceutical Materials*; John Wiley & Sons, 2017; pp 38−47.
(7) Jurczak, E.; Mazurek, A. H.; Szeleszczuk, Ł.; Pisklak, D. M.; Zielińska-Pisklak, M. Pharmaceutical hydrates analysis — overview of methods and recent advances. *Pharmaceutics* **2020**, *12*, No. 959.
(8) Griesser, U. J. The Importance of Solvates. In *Polymorphism in the Pharmaceutical Industry*; Hilfiker, R., Ed.; Wiley-VCH Verlag GmbH & Co. KGaA, 2006; pp 211−233.
(9) Brittain, H. G.; Morris, K. R.; Boerrigter, X. M. Structural Aspects of Solvatomorphic Systems. In *Polymorphism in Pharmaceutical Solids*, 2nd ed.; Brittain, H. G., Ed.; Informa Healthcare USA, Inc., 1999; pp 233−281.
(10) Hossain Mithu, M. S.; Economidou, S.; Trivedi, V.; Bhatt, S.; Douroumis, D. Advanced methodologies for pharmaceutical salt synthesis. *Cryst. Growth Des.* **2021**, *21*, 1358−1374.
(11) Chakravarty, P.; Nagapudi, K. The importance of water-solid interactions in small molecule drug development: an industry perspective. *TrAC,Trends Anal. Chem.* **2021**, *140*, No. 116276.
(12) Shaikh, R.; Singh, R.; Walker, G. M.; Croker, D. M. Pharmaceutical cocrystal drug products: an outlook on product development. *Trends Pharmacol. Sci.* **2018**, *39*, 1033−1048.
(13) Duggirala, N. K.; Perry, M. L.; Almarsson, Ö.; Zaworotko, M. J. Pharmaceutical cocrystals: along the path to improved medicines. *Chem. Commun.* **2016**, *52*, 640−655.
(14) Serajuddin, A. T. M. Salt formation to improve drug solubility. *Adv. Drug Delivery Rev.* **2007**, *59*, 603−616.
(15) Aitipamula, S.; Banerjee, R.; Bansal, A. K.; Biradha, K.; Cheney, M. L.; Choudhury, A. R.; Desiraju, G. R.; Dikundwar, A. G.; Dubey, R.; Duggirala, N.; et al. Polymorphs, salts, and cocrystals: what's in a name? *Cryst. Growth Des.* **2012**, *12*, 2147−2152.
(16) Childs, S. L.; Stahly, G. P.; Park, A. The salt−cocrystal continuum: the influence of crystal structure on ionization state. *Mol. Pharm.* **2007**, *4*, 323−338.
(17) Kersten, K.; Kaura, R.; Matzgera, A. Survey and analysis of crystal polymorphism in organic structures. *IUCrJ* **2018**, *5*, 124−129.
(18) Mnguni, M. J.; Michael, J. P.; Lemmerer, A. Binary polymorphic cocrystals: an update on the available literature in the Cambridge Structural Database, including a new polymorph of the pharmaceutical 1:1 cocrystal theophylline−3,4-dihydroxybenzoic acid. *Acta Crystallogr., Sect. C: Struct. Chem.* **2018**, *74*, 715−720.
(19) Stahly, G. P. Diversity in single- and multiple-component crystals. the search for and prevalence of polymorphs and cocrystals. *Cryst. Growth Des.* **2007**, *7*, 1007−1026.
(20) Tilbury, C. J.; Chen, J.; Mattei, A.; Chen, S.; Sheikh, A. Y. Combining theoretical and data-driven approaches to predict drug substance hydrate formation. *Cryst. Growth Des.* **2018**, *18*, 57−67.
(21) Paulekuhn, G. S.; Dressman, J. B.; Saal, C. Trends in active pharmaceutical ingredient salt selection based on analysis of the orange book database. *J. Med. Chem.* **2007**, *50*, 6665−6672.
(22) Byrn, S. R.; Pfeiffer, R. R.; Stephenson, G.; Grant, D. J. W.; Gleason, W. B. Solid-State Pharmaceutical Chemistry. *Chem. Mater.* **1994**, *6*, 1148−1158.
(23) Bugay, D. E. Characterization of the solid-state: spectroscopic techniques. *Adv. Drug Delivery Rev.* **2001**, *48*, 43−65.
(24) Li, M.; Xu, W.; Su, Y. Solid-state NMR spectroscopy in pharmaceutical sciences. *TrAC, Trends Anal. Chem.* **2021**, *135*, No. 116152.
(25) Harris, R. K. NMR studies of organic polymorphs & solvates. *Analyst* **2006**, *131*, 351−373.
(26) Berendt, R. T.; Sperger, D. M.; Munson, E. J.; Isbester, P. K. Solid-state NMR spectroscopy in pharmaceutical research and analysis. *TrAC, Trends Anal. Chem.* **2006**, *25*, 977−984.
(27) Geppi, M.; Mollica, G.; Borsacchi, S.; Veracini, C. A. Solid-state NMR studies of pharmaceutical systems. *Appl. Spectrosc. Rev.* **2008**, *43*, 202−302.
(28) Vogt, F. G. Evolution of solid-state NMR in pharmaceutical analysis. *Future Med. Chem.* **2010**, *2*, 915−921.
(29) Vogt, F. G. Solid-State NMR in Drug Discovery and Development. In *New Applications of NMR in Drug Discovery and Development*; The Royal Society of Chemistry, 2013; pp 43−100.
(30) Hamaed, H.; Pawlowski, J. M.; Cooper, B. F. T.; Fu, R.; Eichhorn, S. H.; Schurko, R. W. Application of solid-state ^{35}Cl NMR to the structural characterization of hydrochloride pharmaceuticals and their polymorphs. *J. Am. Chem. Soc.* **2008**, *130*, 11056−11065.
(31) Hildebrand, M.; Hamaed, H.; Namespetra, A. M.; Donohue, J. M.; Fu, R.; Hung, I.; Gan, Z.; Schurko, R. W. ^{35}Cl solid-state NMR of HCl salts of active pharmaceutical ingredients: structural prediction, spectral fingerprinting and polymorph recognition. *CrystEngComm* **2014**, *16*, 7334−7356.
(32) Namespetra, A. M.; Hirsh, D. A.; Hildebrand, M. P.; Sandre, A. R.; Hamaed, H.; Rawson, J. M.; Schurko, R. W. ^{35}Cl solid-state NMR spectroscopy of HCl pharmaceuticals and their polymorphs in bulk and dosage forms. *CrystEngComm* **2016**, *18*, 6213−6232.
(33) Hirsh, D. A.; Rossini, A. J.; Emsley, L.; Schurko, R. W. ^{35}Cl dynamic nuclear polarization solid-state NMR of active pharmaceutical ingredients. *Phys. Chem. Chem. Phys.* **2016**, *18*, 25893−25904.
(34) Hirsh, D. A.; Su, Y.; Nie, H.; Xu, W.; Stueber, D.; Variankaval, N.; Schurko, R. W. Quantifying disproportionation in pharmaceutical formulations with ^{35}Cl solid-state NMR. *Mol. Pharm.* **2018**, *15*, 4038−4048.
(35) Hirsh, D. A.; Holmes, S. T.; Chakravarty, P.; Peach, A. A.; DiPasquale, A. G.; Nagapudi, K.; Schurko, R. W. *In situ* characterization of waters of hydration in a variable-hydrate active pharmaceutical ingredient using ^{35}Cl solid-state NMR and X-ray diffraction. *Cryst. Growth Des.* **2019**, *19*, 7349−7362.
(36) Holmes, S. T.; Hook, J. M.; Schurko, R. W. Nutraceuticals in bulk and dosage forms: analysis by ^{35}Cl and ^{14}N solid-state NMR and DFT calculations. *Mol. Pharm.* **2022**, *19*, 440−455.
(37) Iuga, D.; Corlett, E. K.; Brown, S. P. ^{35}Cl-^{1}H heteronuclear correlation MAS NMR experiments for probing pharmaceutical salts. *Magn. Reson. Chem.* **2021**, *59*, 1089−1100.
(38) Peach, A. A.; Hirsh, D. A.; Holmes, S. T.; Schurko, R. W. Mechanochemical syntheses and ^{35}Cl solid-state NMR characterization of fluoxetine HCl cocrystals. *CrystEngComm* **2018**, *20*, 2780−2792.
(39) Vogt, F. G.; Williams, G. R.; Strohmeier, M.; Johnson, M. N.; Copley, R. C. B. Solid-state NMR analysis of a complex crystalline phase of ronacaleret hydrochloride. *J. Phys. Chem. B* **2014**, *118*, 10266−10284.
(40) Vogt, F. G.; Williams, G. R.; Copley, R. C. B. Solid-state NMR analysis of a boron-containing pharmaceutical hydrochloride salt. *J. Pharm. Sci.* **2013**, *102*, 3705−3716.
(41) Pandey, M. K.; Kato, H.; Ishii, Y.; Nishiyama, Y. Two-dimensional proton-detected ^{35}Cl/^{1}H correlation solid-state NMR experiment under fast magic angle sample spinning: application to pharmaceutical compounds. *Phys. Chem. Chem. Phys.* **2016**, *18*, 6209−6216.
(42) Wijesekara, A. V.; Venkatesh, A.; Lampkin, B. J.; VanVeller, B.; Lubach, J. W.; Nagapudi, K.; Hung, I.; Gor'kov, P. L.; Gan, Z.; Rossini, A. J. Fast acquisition of proton-detected HETCOR solid-state NMR spectra of quadrupolar nuclei and rapid measurement of NH bond lengths by frequency selective HMQC and RESPDOR pulse sequences. *Chem. - Eur. J.* **2020**, *26*, 7881−7888.
(43) Bryce, D. L.; Gee, M.; Wasylishen, R. E. High-field chlorine NMR spectroscopy of solid organic hydrochloride salts: a sensitive

https://doi.org/10.1021/acs.cgd.2c01539
Cryst. Growth Des. 2023, 23, 3412−3426

probe of hydrogen bonding environments. *J. Phys. Chem. A* **2001**, *105*, 10413−10421.
(44) Gervais, C.; Dupree, R.; Pike, K. J.; Bonhomme, C.; Profeta, M.; Pickard, C. J.; Mauri, F. Combined first-principles computational and experimental multinuclear solid-state NMR investigation of amino acids. *J. Phys. Chem. A* **2005**, *109*, 6960−6969.
(45) Bryce, D. L.; Sward, G. D.; Adiga, S. Solid-state $^{35/37}$Cl NMR spectroscopy of hydrochloride salts of amino acids implicated in chloride ion transport channel selectivity: opportunities at 900 MHz. *J. Am. Chem. Soc.* **2006**, *128*, 2121−2134.
(46) Bryce, D. L.; Sward, G. D. Chlorine-35/37 NMR spectroscopy of solid amino acid hydrochlorides: refinement of hydrogen-bonded proton positions using experiment and theory. *J. Phys. Chem. B* **2006**, *110*, 26461−26470.
(47) Chapman, R. P.; Bryce, D. L. A high-field solid-state $^{35/37}$Cl NMR and quantum chemical investigation of the chlorine quadrupolar and chemical shift tensors in amino acid hydrochlorides. *Phys. Chem. Chem. Phys.* **2007**, *9*, 6219−6230.
(48) Chapman, R. P.; Hiscock, J. R.; Gale, P. A.; Bryce, D. L. A solid-state $^{35/37}$Cl NMR study of a chloride ion receptor and a GIPAW-DFT study of chlorine NMR interaction tensors in organic hydrochlorides. *Can. J. Chem.* **2011**, *89*, 822−834.
(49) Socha, O.; Hodgkinson, P.; Widdifield, C. M.; Yates, J. R.; Dracinsky, M. Exploring systematic discrepancies in DFT calculations of chlorine nuclear quadrupole couplings. *J. Phys. Chem. A* **2017**, *121*, 4103−4113.
(50) Attrell, R. J.; Widdifield, C. M.; Korobkov, I.; Bryce, D. L. Weak halogen bonding in solid haloanilinium halides probed directly via chlorine-35, bromine-81, and iodine-127 NMR spectroscopy. *Cryst. Growth Des.* **2012**, *12*, 1641−1653.
(51) Penner, G. H.; Webber, R.; O'Dell, L. A. A multinuclear NMR and quantum chemical study of solid trimethylammonium chloride. *Can. J. Chem.* **2011**, *89*, 1036−1046.
(52) Burgess, K. M. N.; Korobkov, I.; Bryce, D. L. A combined solid-state NMR and X-ray crystallography study of the bromide ion environments in triphenylphosphonium bromides. *Chem. - Eur. J.* **2012**, *18*, 5748−5758.
(53) Viger-Gravel, J.; Leclerc, S.; Korobkov, I.; Bryce, D. L. Direct investigation of halogen bonds by solid-state multinuclear magnetic resonance spectroscopy and molecular orbital analysis. *J. Am. Chem. Soc.* **2014**, *136*, 6929−6942.
(54) Vojvodin, C. S.; Holmes, S. T.; Watanabe, L. K.; Rawson, J. M.; Schurko, R. W. Multi-component crystals containing urea: mechanochemical synthesis and characterization by ^{35}Cl solid-state NMR spectroscopy and DFT calculations. *CrystEngComm* **2022**, *24*, 2626−2641.
(55) Azaïs, T.; Bonhomme, C.; Smith, M. E. ^{35}Cl quadrupolar constants obtained by solid-state NMR: study of chlorinated Al−O−P clusters, involving OH···Cl hydrogen bonds. *Solid State Nucl. Magn. Reson.* **2003**, *23*, 14−27.
(56) Szell, P. M. J.; Rehman, Z.; Tatman, B. P.; Hughes, L. P.; Blade, H.; Brown, S. P. Exploring the potential of multinuclear solid-state ^{1}H, ^{13}C, and ^{35}Cl magnetic resonance to characterize static and dynamic disorder in pharmaceutical hydrochlorides. *ChemPhysChem* **2023**, *24*, No. e202200558.
(57) Holmes, S. T.; Vojvodin, C. S.; Veinberg, N.; Iacobelli, E. M.; Hirsh, D. A.; Schurko, R. W. Hydrates of active pharmaceutical ingredients: a ^{35}Cl and ^{2}H solid-state NMR and DFT study. *Solid State Nucl. Magn. Reson.* **2022**, *122*, No. 101837.
(58) Ruiz-Colón, K.; Chavez-Arias, C.; Díaz-Alcalá, J. E.; Martínez, M. A. Xylazine intoxication in humans and its importance as an emerging adulterant in abused drugs: a comprehensive review of the literature. *Forensic Sci. Int.* **2014**, *240*, 1−8.
(59) Zvirgzdins, A.; Mishnev, A.; Actiņš, A. Structure determination of three polymorphs of xylazine from laboratory powder diffraction data. *Acta Crystallogr., Sect. B: Struct. Sci., Cryst. Eng. Mater.* **2014**, *70*, 342−346.
(60) Veidis, M. V.; Orola, L.; Arajs, R. N-(2,6-Dimethyl-anilino)-5,6-dihydro-4H-1,3-thia-zin-3-ium chloride monohydrate. *Acta Crystallogr., Sect. E: Struct. Rep. Online* **2008**, *64*, No. o1062.
(61) Olejniczak, A.; Krūkle-Bērziņa; Katrusiak, A. Pressure-stabilized solvates of xylazine hydrochloride. *Cryst. Growth Des.* **2016**, *16*, 3756−3762.
(62) Bērziņš, A.; Krūkle, K.; Actiņš, A.; Kreišmanis, J. P. The relative stability of xylazine hydrochloride polymorphous forms. *Pharm. Dev. Technol.* **2010**, *15*, 217−222.
(63) Krūkle-Bērziņa, K.; Actiņš, A.; Bērziņš, A. Hydration of xylazine hydrochloride polymorphic forms A, Z and M. *Latv. J. Chem.* **2011**, *50*, 73−84.
(64) APEXIII, SAINT, SADABS; Madison, Wisconsin, USA, 2016.
(65) Sheldrick, G. M. SHELXT - Integrated space-group and crystal-structure determination. *Acta Crystallogr., Sect. A: Found. Adv.* **2015**, *71*, 3−8.
(66) Sheldrick, G. M. Crystal structure refinement with SHELXL. *Acta Crystallogr., Sect. C: Struct. Chem.* **2015**, *71*, 3−8.
(67) Dolomanov, O. V.; Bourhis, L. J.; Gildea, R. J.; Howard, J. A. K.; Puschmann, H. OLEX2: a complete structure solution, refinement and analysis program. *J. Appl. Crystallogr.* **2009**, *42*, 339−341.
(68) Peersen, O. B.; Wu, X. L.; Kustanovich, I.; Smith, S. O. Variable-amplitude cross-polarization MAS NMR. *J. Magn. Reson., Ser. A* **1993**, *104*, 334−339.
(69) Metz, G.; Wu, X. L.; Smith, S. O. Ramped-amplitude pross Polarization in magic-angle-spinning NMR. *J. Magn. Reson., Ser. A* **1994**, *110*, 219−227.
(70) Schaefer, J.; Stejskal, E. O. Carbon-13 nuclear magnetic resonance of polymers spinning at the magic angle. *J. Am. Chem. Soc.* **1976**, *98*, 1031−1032.
(71) Pines, A.; Waugh, J. S.; Gibby, M. G. Proton-enhanced nuclear induction spectroscopy. 13C chemical shielding anisotropy in some organic solids. *Chem. Phys. Lett.* **1972**, *15*, 373−376.
(72) Potrzebowski, M. J.; Tekely, P.; Dusausoy, Y. Comment to ^{13}C-NMR studies of α and γ polymorphs of glycine. *Solid State Nucl. Magn. Reson.* **1998**, *11*, 253−257.
(73) Taylor, R. E. Setting up ^{13}C CP/MAS experiments. *Concepts Magn. Reson., Part A* **2004**, *22A*, 37−49.
(74) Hahn, E. L. Spin echoes. *Phys. Rev.* **1950**, *80*, 580−594.
(75) Larsen, F. H.; Jakobsen, H. J.; Ellis, P. D.; Nielsen, N. C. QCPMG-MAS NMR of half-integer quadrupolar nuclei. *J. Magn. Reson.* **1998**, *131*, 144−147.
(76) O'Dell, L. A.; Rossini, A. J.; Schurko, R. W. Acquisition of ultra-wideline NMR spectra from quadrupolar nuclei by frequency stepped WURST−QCPMG. *Chem. Phys. Lett.* **2009**, *468*, 330−335.
(77) O'Dell, L. A.; Schurko, R. W. QCPMG using adiabatic pulses for faster acquisition of ultra-wideline NMR spectra. *Chem. Phys. Lett.* **2008**, *464*, 97−102.
(78) Bhattacharyya, R.; Frydman, L. Quadrupolar nuclear magnetic resonance spectroscopy in solids using frequency-swept echoing pulses. *J. Chem. Phys.* **2007**, *127*, No. 194503.
(79) Kupce, E.; Freeman, R. Adiabatic pulses for wideband inversion and broadband decoupling. *J. Magn. Reson., Ser. A* **1995**, *115*, 273−276.
(80) Yao, Z.; Kwak, H.-T.; Sakellariou, D.; Emsley, L.; Grandinetti, P. J. Sensitivity enhancement of the central transition NMR signal of quadrupolar nuclei under magic-angle spinning. *Chem. Phys. Lett.* **2000**, *327*, 85−90.
(81) O'Dell, L. A. The WURST kind of pulses in solid-state NMR. *Solid State Nucl. Magn. Reson.* **2013**, *55*−*56*, 28−41.
(82) van Meerten, S. G. J.; Franssen, W. M. J.; Kentgens, A. P. M. ssNake: a cross-platform open-source NMR data processing and fitting application. *J. Magn. Reson.* **2019**, *301*, 56−66.
(83) Adiga, S.; Aebi, D.; Bryce, D. L. EFGShield — a program for parsing and summarizing the results of electric field gradient and nuclear magnetic shielding tensor calculations. *Can. J. Chem.* **2007**, *85*, 496−505.

https://doi.org/10.1021/acs.cgd.2c01539
Cryst. Growth Des. 2023, 23, 3412−3426

(84) Clark, S. J.; Segall, M. D.; Pickard, C. J.; Hasnip, P. J.; Probert, M. J.; Refson, K.; Payne, M. C. First principles methods using CASTEP. *Z. Kristallogr. - Cryst. Mater.* **2005**, *220*, 567−570.
(85) Hammer, B.; Hansen, L. B.; Nørskov, J. K. Improved adsorption energetics within density-functional theory using revised Perdew-Burke-Ernzerhof functionals. *Phys. Rev. B* **1999**, *59*, 7413−7421.
(86) Yates, J. R.; Pickard, C. J.; Mauri, F. Calculation of NMR chemical shifts for extended systems using ultrasoft pseudopotentials. *Phys. Rev. B* **2007**, *76*, No. 024401.
(87) Monkhorst, H. J.; Pack, J. D. Special points for Brillouin-zone integrations. *Phys. Rev. B* **1976**, *13*, 5188−5192.
(88) Grimme, S. Semiempirical GGA-type density functional constructed with a long-range dispersion correction. *J. Comput. Chem.* **2006**, *27*, 1787−1799.
(89) Holmes, S. T.; Iuliucci, R. J.; Mueller, K. T.; Dybowski, C. Semi-empirical refinements of crystal structures using ^{17}O quadrupolar-coupling tensors. *J. Chem. Phys.* **2017**, *146*, No. 064201.
(90) Holmes, S. T.; Schurko, R. W. Refining crystal structures with quadrupolar NMR and dispersion-corrected density functional theory. *J. Phys. Chem. C* **2018**, *122*, 1809−1820.
(91) Holmes, S. T.; Vojvodin, C. S.; Schurko, R. W. Dispersion-corrected DFT methods for applications in nuclear magnetic resonance crystallography. *J. Phys. Chem. A* **2020**, *124*, 10312−10323.
(92) Pfrommer, B. G.; Côté, M.; Louie, S. G.; Cohen, M. L. Relaxation of crystals with the quasi-Newton method. *J. Comput. Phys.* **1997**, *131*, 233−240.
(93) Pickard, C. J.; Mauri, F. All-electron magnetic response with pseudopotentials: NMR chemical shifts. *Phys. Rev. B* **2001**, *63*, No. 245101.
(94) Vojvodin, C. S.; Holmes, S. T.; Watanabe, L. K.; Rawson, J. M.; Schurko, R. W. Multi-component crystals containing urea: mechanochemical synthesis and characterization by ^{35}Cl solid-state NMR spectroscopy and DFT calculations. *CrystEngComm* **2022**, *24*, 2626−2641.
(95) Krūkle-Bērziņa, K.; Actiņš, A. Powder X-ray diffraction investigation of xylazine hydrochloride solid phase transformation kinetics. *Int. J. Chem. Kinet.* **2014**, *46*, 161−168.
(96) Bērziņš, A.; Actiņš, A.; P Kreišmanis, J. Hydration and dehydration kinetics of xylazine hydrochloride. *Pharm. Dev. Technol.* **2009**, *14*, 388−399.
(97) Jean-Claude Bradley Open Melting Point Dataset, https://figshare.com/articles/dataset/Jean_Claude_Bradley_Open_Melting_Point_Datset/1031637.
(98) Holmes, S. T.; Engl, O. G.; Srnec, M. N.; Madura, J. D.; Quiñones, R.; Harper, J. K.; Schurko, R. W.; Iuliucci, R. J. Chemical shift tensors of cimetidine form A modeled with density functional theory calculations: implications for NMR crystallography. *J. Phys. Chem. A* **2020**, *124*, 3109−3119.
(99) Fenzke, D.; Freude, D.; Fröhlich, T.; Haase, J. NMR intensity measurements of half-integer quadrupole nuclei. *Chem. Phys. Lett.* **1984**, *111*, 171−175.
(100) Steiner, T. Hydrogen-bond distances to halide ions in organic and organometallic crystal structures: up-to-date database study. *Acta Crystallogr., Sect. B: Struct. Sci.* **1998**, *54*, 456−463.
(101) Desiraju, G. R.; Steiner, T. *The Weak Hydrogen Bond in Structural Chemistry and Biology*; Oxford University Press, Inc., 1999.
(102) Steiner, T. The hydrogen bond in the solid state. *Angew. Chem., Int. Ed.* **2002**, *41*, 48−76.
(103) Pyykkö, P. Year-2017 nuclear quadrupole moments. *Mol. Phys.* **2018**, *116*, 1328−1338.
(104) Paruzzo, F. M.; Hofstetter, A.; Musil, F.; De, S.; Ceriotti, M.; Emsley, L. Chemical shifts in molecular solids by machine learning. *Nat. Commun.* **2018**, *9*, No. 4501.
(105) Cordova, M.; Engel, E. A.; Stefaniuk, A.; Paruzzo, F.; Hofstetter, A.; Ceriotti, M.; Emsley, L. A machine learning model of chemical shifts for chemically and structurally diverse molecular solids. *J. Phys. Chem. C* **2022**, *126*, 16710−16720.
(106) Sun, H.; Dwaraknath, S.; Ling, H.; Qu, X.; Huck, P.; Persson, K. A.; Hayes, S. E. Enabling materials informatics for ^{29}Si solid-state NMR of crystalline materials. *npj Comput. Mater.* **2020**, *6*, No. 53.

https://doi.org/10.1021/acs.cgd.2c01539
Cryst. Growth Des. 2023, 23, 3412−3426